

# Structural insights into the mechanism of the sodium/iodide symporter

<https://doi.org/10.1038/s41586-022-05530-2>

Received: 17 May 2022

Accepted: 4 November 2022

Published online: 14 December 2022

 Check for updates

Silvia Ravera<sup>1</sup>, Juan Pablo Nicola<sup>2</sup>, Glicella Salazar-De Simone<sup>3</sup>, Fred J. Sigworth<sup>4</sup>, Erkan Karakas<sup>1</sup>, L. Mario Amzel<sup>5,7</sup>, Mario A. Bianchet<sup>5,6</sup> & Nancy Carrasco<sup>1</sup>✉

The sodium/iodide symporter (NIS) is the essential plasma membrane protein that mediates active iodide ( $I^-$ ) transport into the thyroid gland, the first step in the biosynthesis of the thyroid hormones—the master regulators of intermediary metabolism. NIS couples the inward translocation of  $I^-$  against its electrochemical gradient to the inward transport of  $Na^+$  down its electrochemical gradient<sup>1,2</sup>. For nearly 50 years before its molecular identification<sup>3</sup>, NIS was the molecule at the centre of the single most effective internal radiation cancer therapy: radioiodide ( $^{131}I^-$ ) treatment for thyroid cancer<sup>2</sup>. Mutations in NIS cause congenital hypothyroidism, which must be treated immediately after birth to prevent stunted growth and cognitive deficiency<sup>2</sup>. Here we report three structures of rat NIS, determined by single-particle cryo-electron microscopy: one with no substrates bound; one with two  $Na^+$  and one  $I^-$  bound; and one with one  $Na^+$  and the oxyanion perrhenate bound. Structural analyses, functional characterization and computational studies show the substrate-binding sites and key residues for transport activity. Our results yield insights into how NIS selects, couples and translocates anions—thereby establishing a framework for understanding NIS function—and how it transports different substrates with different stoichiometries and releases substrates from its substrate-binding cavity into the cytosol.

Iodide ( $I^-$ ) is a key micronutrient because its oxidized form, iodine, is an essential constituent of the thyroid hormones. An adequate supply of  $I^-$  early in life is crucial for prevention of  $I^-$  deficiency disorders (IDDs), because the thyroid hormones are critical for embryonic and postembryonic development, particularly that of the central nervous system, lungs and musculoskeletal system. The thyroid hormones are also master regulators of cellular metabolism in virtually all tissues at all stages of life<sup>4,5</sup>. The first step in the biosynthesis of the thyroid hormones is the active transport of  $I^-$  into the thyroid, which is mediated by the product of the *SLC5A5* gene—the sodium/iodide symporter (NIS), an intrinsic plasma membrane protein located at the basolateral surface of the thyroid follicular cells. NIS couples the inward translocation of  $I^-$  against its electrochemical gradient to the inward transport of  $Na^+$  down its electrochemical gradient<sup>3</sup>. A notable function of NIS is that—unlike  $Cl^-$  channels and transporters, which transport both  $Cl^-$  and  $I^-$  (with affinities in the millimolar range)<sup>5</sup>—NIS discriminates between these two anions in a way that is of great physiological significance: it transports  $I^-$  but not  $Cl^-$ , even though the concentration of  $Cl^-$  in the extracellular milieu (around 100 mM) is over 10<sup>5</sup> times that of  $I^-$  (under 1  $\mu$ M). Notable mechanistic insights have been gained by determination of how NIS mutations found in patients with IDDs affect the folding of the protein, plasma membrane targeting and activity<sup>2,6</sup>.

NIS is also the molecule at the centre of the successful treatment for thyroid cancer based on  $^{131}I^-$ , administered after thyroidectomy; this therapy targets remnant malignant cells and metastases that

actively accumulate the radioisotope via NIS. In addition, NIS is functionally expressed endogenously not only in several extrathyroidal tissues—such as the salivary glands, stomach, intestine and lactating breast—but also in primary and metastatic breast cancers<sup>7</sup>. This last finding opens up the possibility that NIS-mediated  $^{131}I^-$  treatment could be used against breast cancer. Furthermore, there is great interest<sup>2</sup> in the expression of NIS exogenously in cancers that do not express it endogenously, to render them susceptible to destruction by  $^{131}I^-$  (refs.<sup>8,9</sup>).

NIS translocates several substrates other than  $I^-$ , including oxyanions such as the environmental pollutant perchlorate ( $ClO_4^-$ ) and the imaging substrates pertechnetate ( $^{99m}TcO_4^-$ ) and perrhenate ( $^{186}ReO_4^-$ ,  $^{188}ReO_4^-$ ), which are used in single-photon emission computed tomography (SPECT). The NIS substrates tetrafluoroborate ( $^{18}F-BF_4^-$ ) and  $^{124}I^-$  are used in positron emission tomography (PET). NIS is now becoming the counterpart of green fluorescent protein or luciferase for imaging studies in humans<sup>2,8,10,11</sup>. Although the physiology, biochemistry, biophysics and cell biology of NIS have all been investigated extensively<sup>2</sup>, our understanding of its symport mechanism has, until now, been hindered by a lack of high-resolution structures of NIS. Here, we use single-particle cryo-electron microscopy (cryo-EM), molecular dynamics simulations and functional studies to gain a structural understanding of how NIS binds its anion substrates with such high affinity, how it translocates anions and how mutations in NIS lead to congenital IDDs.

<sup>1</sup>Department of Molecular Physiology and Biophysics, Vanderbilt University, Nashville, TN, USA. <sup>2</sup>Department of Clinical Biochemistry, National University of Córdoba, Córdoba, Argentina.

<sup>3</sup>Department of Obstetrics and Gynecology, Columbia University Medical Center, New York, NY, USA. <sup>4</sup>Department of Cellular and Molecular Physiology, Yale School of Medicine, New Haven, CT, USA. <sup>5</sup>Department of Biophysics and Biophysical Chemistry, Johns Hopkins University School of Medicine, Baltimore, MD, USA. <sup>6</sup>Department of Neurology, Johns Hopkins University School of Medicine, Baltimore, MD, USA. <sup>7</sup>Deceased: L. Mario Amzel. <sup>✉</sup>e-mail: nancy.carrasco@vanderbilt.edu

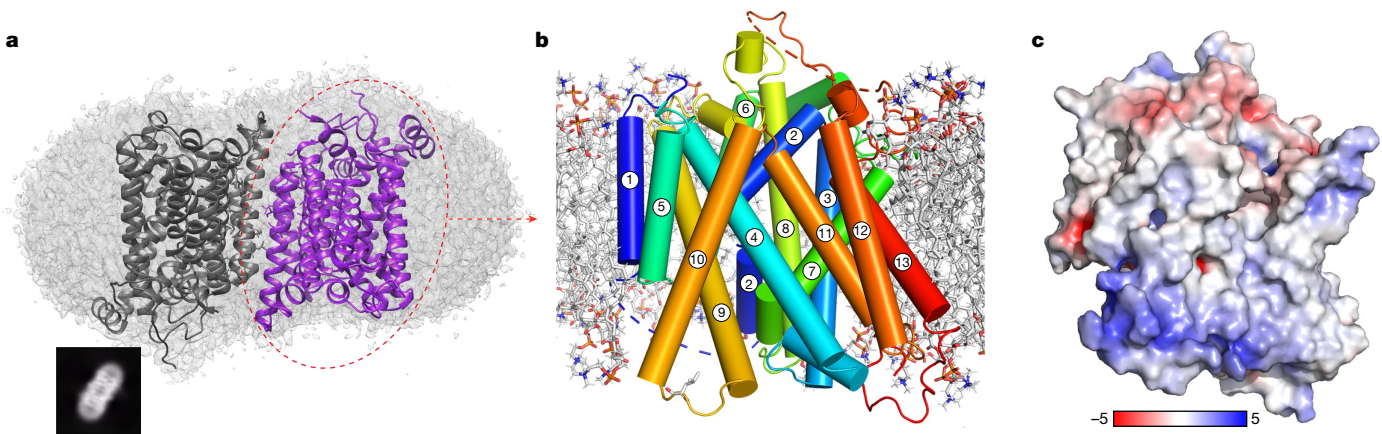


**Fig. 1 | Structure of NIS.** **a**, Two NIS molecules entirely embedded in a detergent micelle, side view. An example of two-dimensional (2D) classes representing the corresponding view is shown in the black square. **b**, NIS structure viewed from the plane of the membrane, with numbered TM helices

depicted as cylinders. **c**, Side view of NIS as in **a** but with solvent-accessible surface coloured according to the electrostatic potential in  $k_B T/e$ , in which  $k_B$  denotes the Boltzmann's constant,  $T$  denotes absolute temperature, and  $e$  denotes elementary charge (red, negative; blue, positive).

## Structure determination

Rat NIS shares 89% sequence identity with human NIS (Supplementary Fig. 2) and has similar transport properties<sup>6,12–14</sup>. We have previously shown that glycosylation is not required for NIS activity<sup>12,15</sup>. Hence, to carry out structural studies, we engineered a complementary DNA coding for a recombinant unglycosylated full-length rat NIS molecule: a triple NIS mutant in which all three Asn residues that are glycosylated were replaced with Gln (N225Q/N485Q/N497Q), with a human influenza hemagglutinin (HA) tag at the N terminus and His and streptavidin-binding protein tags at the C terminus (recombinant tagged NIS, T-NIS). We expressed T-NIS in 293F cells, enriched for cells expressing the protein by flow cytometry with an anti-HA antibody, and demonstrated that its activity is indistinguishable from that of wild-type NIS (Extended Data Fig. 1a–c). We then solubilized and purified T-NIS. The protein that eluted in the peak fraction and electrophoresed as a single polypeptide was used to determine the structure of NIS by single-particle cryo-EM (Extended Data Table 1 and Extended Data Fig. 1d–k).

The cryo-EM map (overall resolution 3.46 Å) shows that NIS in the micelles assumes a dimeric conformation with excellent density for all 26 transmembrane segments (TMSs), as well as for significant regions of the extramembrane loops and 17 out of 74 residues in the C terminus. Well-resolved TMSs of varying length show clearly visible  $\alpha$ -helical features (Extended Data Fig. 2a). As a result, the map enabled us to build a model of the entire protein from residues 9 to 561, with the exception of the loops between TMSs 1 and 2 (residues 34–52), TMSs 5 and 6 (residues 183–188) and TMSs 12 and 13 (residues 483–510), whose lack of density may be attributable to the high flexibility of these regions. To further improve the quality of the map, we applied a symmetry expansion to the particles and carried out local refinement with a mask designed for a single monomer, yielding a new map at 3.30 Å resolution (Extended Data Fig. 1k).

The NIS dimers embedded in each micelle are in an antiparallel configuration (Fig. 1a and Extended Data Figs. 1a and 2b). As we have demonstrated, when NIS is endogenously expressed its N terminus faces the extracellular milieu and its C terminus the cytosol<sup>12,13,15–17</sup>. Thus it is extremely unlikely that antiparallel NIS dimers in the micelles are physiological. Instead, the antiparallel configuration resulted from the solubilization and purification process. The two oppositely oriented monomers interact through a twofold axis perpendicular to TMS 5 and TMS 10, and to their local symmetry counterparts. No salt

bridges were observed at the interface and there are only two symmetrical pairs of polar residues across the local symmetry axis—S396 and T400—but they do not appear to contribute to formation of the dimer by means of hydrogen bonds or water-mediated interactions. Only apolar interactions hold the dimer together. Duplicated by the local symmetry, aromatic stacking of W165 between F385 and F392 in the other monomer allows for the specific interaction required to generate identical dimers in different micelles (Extended Data Fig. 2c).

As predicted<sup>14,18</sup>, NIS has a LeuT fold with two 5-helix bundle domains (TMSs 2–6 and 7–11) related by an internal pseudo-two-fold symmetry around an axis through the centre of the transporter and perpendicular to the plane of the membrane (Fig. 1b, Extended Data Fig. 1a and Supplementary Fig. 3). This conserved molecular architecture is common to various membrane transporters that have unrelated sequences and belong to different families<sup>19–22</sup>. The alignment between the two repeats has a root mean square deviation (RMSD) value of 3.01 Å for 115 Cα atoms aligned (LeuTRMSD 5.3 Å for 130 Cα atoms<sup>23</sup>). TMSs 2–6 are related to TMSs 7–11 by a 178° rotation parallel to the membrane plane. TMSs 2 and 7 have unwound regions (S66–A70 and G261–A263), which probably bind ions and/or participate in the conformational changes that occur during the transport cycle. Analysis of the secondary structure motifs showed the presence of  $\pi$ -helices at three positions: 101–105, 247–251 and 366–371. Although the protein was purified in the presence of a high concentration of Na<sup>+</sup> (350 mM), we refer to this structure as apo-NIS because it does not contain any densities attributable to bound ions.

The electrostatic potential surface shows that the distribution of charges satisfies the positive-inside rule of transmembrane protein topology (Fig. 1c). NIS adopts an inward-facing conformation similar to those observed for the *Vibrio cholerae* Na<sup>+</sup>/galactose transporter (vSGLT)<sup>24</sup> and human Na<sup>+</sup>/glucose transporter 1 (hSGLT1)<sup>21</sup>, and opposite to that of the outwardly open hSGLT2 (ref. <sup>22</sup>) (Supplementary Fig. 4) (Cα RMSD: 2.9 Å over 313 residues, 3.3 Å over 378 residues and 3.75 Å over 363 residues). Although the opening is narrower than that in vSGLT or hSGLT1, the positions of the TMSs of NIS suggest that the conformation is inwardly open.

## Iodide- and sodium-binding sites

To determine how NIS binds I<sup>−</sup> with such high affinity, we determined the structure of NIS with I<sup>−</sup> bound to it at 3.12 Å (Extended Data Fig. 3a). We observed three additional nonprotein densities in the core of the

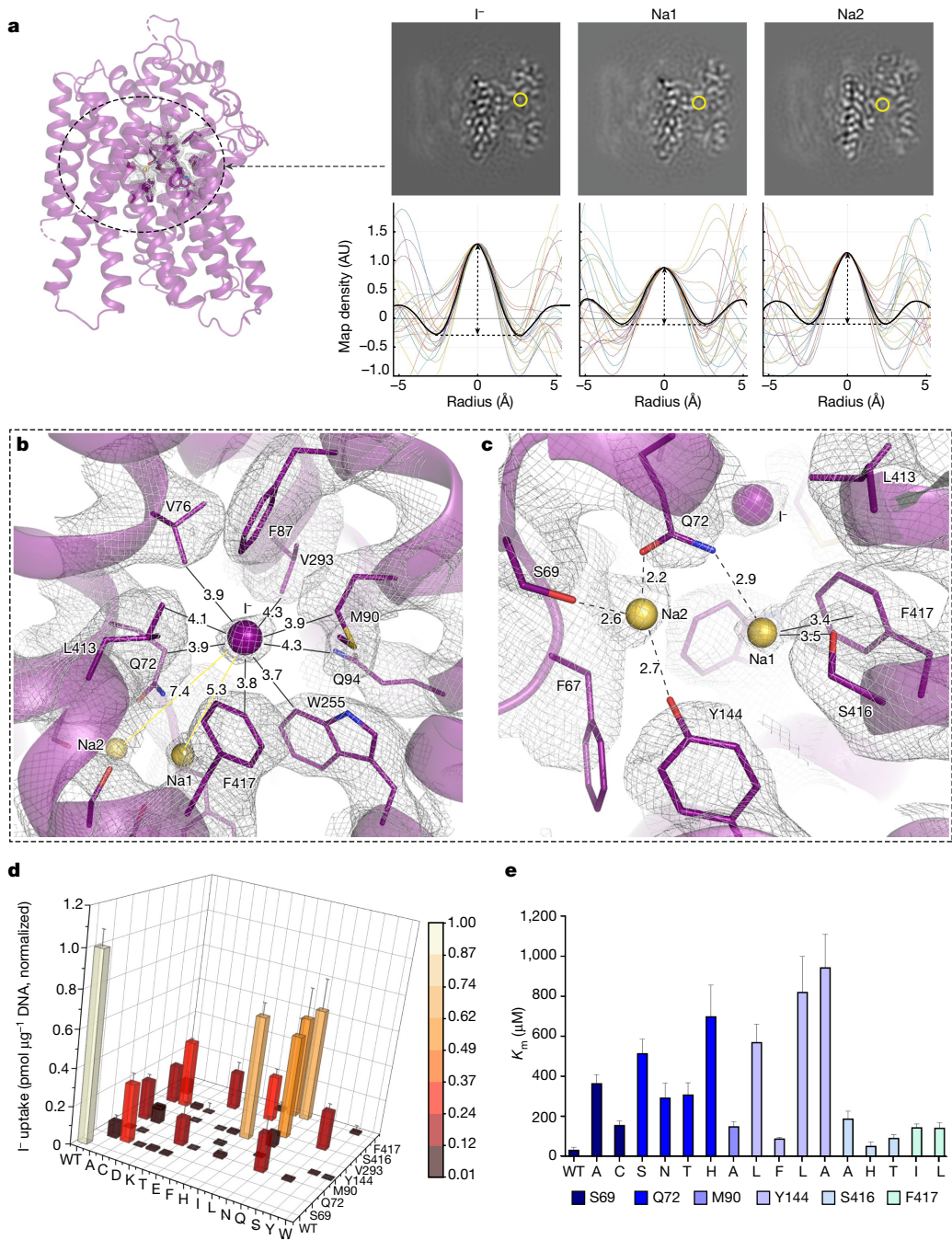


**Fig. 2 | Iodide- and sodium-binding sites.** **a**, Top, in the NIS-I<sup>-</sup> structure the yellow circle indicates the substrate-binding pocket. Ions transported by NIS were identified by analysis of map density values (map slices) along 24 lines passing through each site, circled in yellow. Bottom, map values are plotted for each line and the spherically averaged mean is plotted in black. **b**, Close-up of the I<sup>-</sup>-binding pocket, where I<sup>-</sup> is represented by the purple sphere. The distance (in Å) from I<sup>-</sup> to each surrounding residue is indicated. Yellow spheres represent sodium ions. **c**, Close-up of interactions between Na1 and Na2 and surrounding

residues. **d**, Functional effects of mutations in binding-site residues. Steady-state transport was determined at 20 μM I<sup>-</sup> and 140 mM Na<sup>+</sup> for 30 min, normalized to values obtained with wild-type NIS (values were obtained in the presence of ClO<sub>4</sub><sup>-</sup>, with those less than 10% of the values obtained in its absence having already been subtracted). Data are mean and s.e.m. from two or three different experiments, each of which was carried out in triplicate ( $n \geq 6$ ). **e**, Michaelis constant ( $K_m$ ) values obtained from the kinetic analysis of I<sup>-</sup> transport; results expressed as mean ± s.d. ( $n \geq 6$ ).

NIS-I<sup>-</sup> map that correspond to the substrates. To assign the correct ion to each position, we plotted the density map in the vicinity of each ion site and generated a sphere with a radius of 5 Å from the density centre. Starting at an ion position, the map density (which is proportional to the electrostatic potential) was ascertained along 48 radial lines in uniformly distributed directions. The radial density, given as the mean over all angles, is plotted as a black curve (Fig. 2a). The height and width

of the peaks are expected to reflect the size of the ions: the positive central peak tends to reflect the nuclear charge and the width of the peak corresponds to the spatial extent of the ion's electron density<sup>25</sup>. The undershoot reflects the potential outside the valence electrons and will be more negative for an anion. Thus, we conclude that the largest peak (1.5 arbitrary units (AU)) corresponds to putative I<sup>-</sup> and the smaller peaks (1.0 and 1.2 AU) to putative Na<sup>+</sup> (Fig. 2a).

The  $\text{I}^-$ -binding site is delimited by residues Q72, V76, M90, Q94, W255, V293, L413 and F417 (Fig. 2b) and has a partially positively charged electrostatic surface potential (Extended Data Fig. 4) that further stabilizes the anion. All these residues are 100% conserved from humans to fish (Supplementary Fig. 2); notably, most are hydrophobic.

In addition to the density in NIS- $\text{I}^-$  ascribed to  $\text{I}^-$ , two other clear densities were present, which we attribute to  $\text{Na}^+$  ions. One of them, which we dubbed Na1 because it is closer to the  $\text{I}^-$  (5.3 Å), interacts with Q72 and S416 and is stabilized by a cation-π interaction with the aromatic ring of F417 (Fig. 2c). By contrast, the other  $\text{Na}^+$ —which we named Na2 (7.4 Å from  $\text{I}^-$ )—is coordinated by the side-chain oxygen atoms of three residues: S69, Q72 and Y144 (Fig. 2c).

To ascertain the functional relevance of the interactions observed, we engineered several amino acid substitutions at positions 69, 72, 90, 94, 144, 293, 416 and 417. In all cases,  $\text{I}^-$  transport at steady state (20  $\mu\text{M}$   $\text{I}^-$ ) was substantially reduced and no  $\text{I}^-$  was transported at all when the substituted residues were charged (Fig. 2d). Similar results have been reported with substitutions at some of these positions in human NIS<sup>26</sup>. Here we show that the effects of the replacements were clearly not due to impaired NIS mutant protein expression or trafficking to the cell surface, because all mutants were present at the plasma membrane at levels comparable to those of wild-type NIS, as determined by flow cytometry with an antibody against the extracellularly facing HA tag (Extended Data Fig. 1a and Supplementary Fig. 5). Increasing the concentration of  $\text{I}^-$  tenfold (to 200  $\mu\text{M}$   $\text{I}^-$ ) caused  $\text{I}^-$  accumulation by wild-type NIS to increase by two- to threefold but had a more pronounced effect on the mutants, whose  $\text{I}^-$  accumulation increased by three- to 20-fold (Extended Data Fig. 5), suggesting that the mutants had a markedly lower affinity for  $\text{I}^-$  than wild-type NIS. To test this hypothesis, we carried out  $\text{I}^-$  transport assays at initial rates. Indeed, the  $K_m$  values of the mutants for  $\text{I}^-$  were considerably higher (3- to 30-fold) than that of wild-type NIS (20–30  $\mu\text{M}$ ) (Fig. 2e and Extended Data Fig. 5). All mutant NIS proteins also had a higher  $K_m$  for  $\text{Na}^+$  than wild-type NIS (50 mM) (Extended Data Fig. 5). These data are consistent with the fact that the binding of one of the substrates increases the affinity of NIS for the other<sup>27,28</sup>.

## Oxyanion-binding site

Although NIS discriminates finely between  $\text{I}^-$  and the other halides, it does translocate substrates other than  $\text{I}^-$ , including the oxyanions  $^{99m}\text{TcO}_4^-$ ,  $\text{ReO}_4^-$  and  $\text{ClO}_4^-$  (an environmental pollutant)<sup>2,7,29–31</sup>. Notably, whereas NIS transports  $\text{I}^-$  electrogenically (with a 2:1  $\text{Na}^+:\text{I}^-$  stoichiometry)<sup>32</sup>, it transports oxyanions electroneutrally (with a 1:1  $\text{Na}^+:\text{oxyanion}$  stoichiometry)<sup>14,27,33</sup>. To deepen our understanding of oxyanion transport by NIS, we determined the structure of the protein in complex with  $\text{ReO}_4^-$  at a resolution of 3.15 Å (Extended Data Fig. 3b). We observed two densities located at approximately the same position as two of the three densities in the NIS- $\text{I}^-$  map. We propose, based on an analysis similar to that carried out for the NIS- $\text{I}^-$  structure (Fig. 2a), that the large density corresponds to  $\text{ReO}_4^-$  owing to the size (2 AU) and shape of the peak, and the small one (1 AU) to  $\text{Na}^+$  (Extended Data Fig. 6).

$\text{ReO}_4^-$  forms hydrogen bonds with Q72 (2.5 Å) and Q94 (2.8 Å) and is in close contact (below 3.6 Å) with V76, M90, W255, V293 and F417 (Fig. 3a). A  $\text{Na}^+$  is located in a position very similar to that occupied by Na1 in the NIS- $\text{I}^-$  structure, and it interacts with the same residues: Q72, S416 and F417 (Fig. 3a). No other density was found that could be attributed to a second  $\text{Na}^+$ , which is consistent with the 1:1 stoichiometry of NIS-mediated oxyanion transport<sup>7,14,27,29,31,33,34</sup>. Although the charge centre distance between the cation and oxyanion is the same as that between  $\text{I}^-$  and Na1 (5.3 Å), the distance between Na1 and a  $\text{ReO}_4^-$  oxygen atom is shorter (3.9 Å). The fact that the amino acids shown to coordinate  $\text{ReO}_4^-$  play a significant role in oxyanion transport was demonstrated by the effects of amino acid substitutions on  $\text{ReO}_4^-$  transport (Extended Data Figs. 6b and 7a–d). A detailed

analysis of the Q72 mutants showed that NIS with Ala, Cys, Glu or His at this position does not transport  $\text{ReO}_4^-$  at a concentration of 3  $\mu\text{M}$ . However, these mutants do transport a modest amount of  $\text{ReO}_4^-$  when its concentration is increased tenfold. In agreement with these data, the  $K_m$  value of Q72H NIS for  $\text{ReO}_4^-$  was tenfold that of wild-type NIS (Extended Data Fig. 7e,f).

## Proposed mechanism of transport by NIS

The NIS- $\text{ReO}_4^-$  structure has a Gln rotamer at position 72 (Fig. 3b and Supplementary Fig. 10) that is different from that in the NIS- $\text{I}^-$  structure. As a result, Q72 interacts with  $\text{ReO}_4^-$  through its amino group and with  $\text{Na}^+$  at the Na1 site through its carbonyl group (which in NIS- $\text{I}^-$  interacts with  $\text{Na}^+$  at the Na2 site). This movement of Q72 might explain, at least in part, the absence of  $\text{Na}^+$  at the Na2 site in the NIS- $\text{ReO}_4^-$  structure and, as a consequence, the electroneutral stoichiometry of  $\text{Na}^+/\text{ReO}_4^-$  transport.

The three NIS structures are remarkably similar. The small RMSDs between the apo and ion-bound structures (0.86 Å for NIS- $\text{I}^-$  and 1.0 Å for NIS- $\text{ReO}_4^-$ ) for 495 Cα atoms aligned suggest that binding of the ions to NIS causes only small, localized changes. Of these structural changes, the most significant occur in the TMS2 kink between F66 and Q72. In the apo structure, this kink is stabilized by hydrogen bonds between the amino group of Q72 and the hydroxyl group of S69 and between the former and the main chain carbonyl of F67, as well as by a stacking interaction between the aliphatic portion of the side chain of Q72 and the aromatic ring of F67. The kink is further stabilized by a hydrogen bond formed between Y144, in the adjacent TMS4, and the main chain carbonyl of S66 (Fig. 4a).

In the NIS- $\text{I}^-$  structure, these kink-stabilizing residues are rearranged to coordinate the  $\text{Na}^+$  ions. Q72 flips from its position in the apo conformation to coordinate Na2 with its amide oxygen and Na1 with its amide nitrogen (Figs. 2b,c and 4a). The aromatic ring of F417 stabilizes Na1 through a cation-π interaction (Figs. 2c and 4a). It is possible that Na1, which appears to be coordinated to a lesser extent than Na2, is also stabilized by the negative charge of the anion. These rearrangements of the TMS2 kink make F67 swing by around 100° away from the inside of the anion-binding pocket to the cytosolic side of the substrate site. In the NIS- $\text{ReO}_4^-$  structure the changes in the TMS2 kink are more pronounced. The backbone atoms of F67 also move 2 Å away from the centre, and M68 rotates approximately 115° upward from the position it has in both the apo-NIS and NIS- $\text{I}^-$  structures (Fig. 3c and Supplementary Fig. 10). Given the position of the carbonyl of F67, and because amino acid substitutions at position 67 reduce transport of  $\text{I}^-$  more than that of  $\text{ReO}_4^-$  (Supplementary Fig. 6), we can speculate that the local rearrangements brought about by replacements interfere with the coordination of Na2 and, consequently,  $\text{ReO}_4^-$  transport should be less affected. Notably, other residues in the structures with substrates bound do not occupy positions significantly different from those in the apo-NIS structure.

Using Caver-Analyst software<sup>35</sup> we identified in the apo-NIS structure, which is inwardly open, a hydrophilic tunnel (with a bottleneck radius of 1.5 Å) that connects the substrate-binding cavity to the cytosol (Fig. 3d). This tunnel is delimited by TMSs 2, 4, 7 and 9 and is lined by some of the residues known to be important for NIS function<sup>36</sup> and also by others reported to be mutated in patients with congenital hypothyroidism due to mutations in NIS. In the apo structure, the ring of F67 partially occupies the anion-binding pocket. By contrast, in the substrate-bound NIS structures the tunnel between the substrate-binding cavity and exit pathway is blocked by the side chain of F67, suggesting that these NIS structures are in an occluded conformation (Fig. 3d).

We ran molecular dynamics simulations with the NIS- $\text{I}^-$  structure, restraining the cations bound to the site observed in the experimental structure (Supplementary Fig. 7a). Both cations form intermolecular bonds with NIS: Na1 participates in a strong cation-π bond, shown

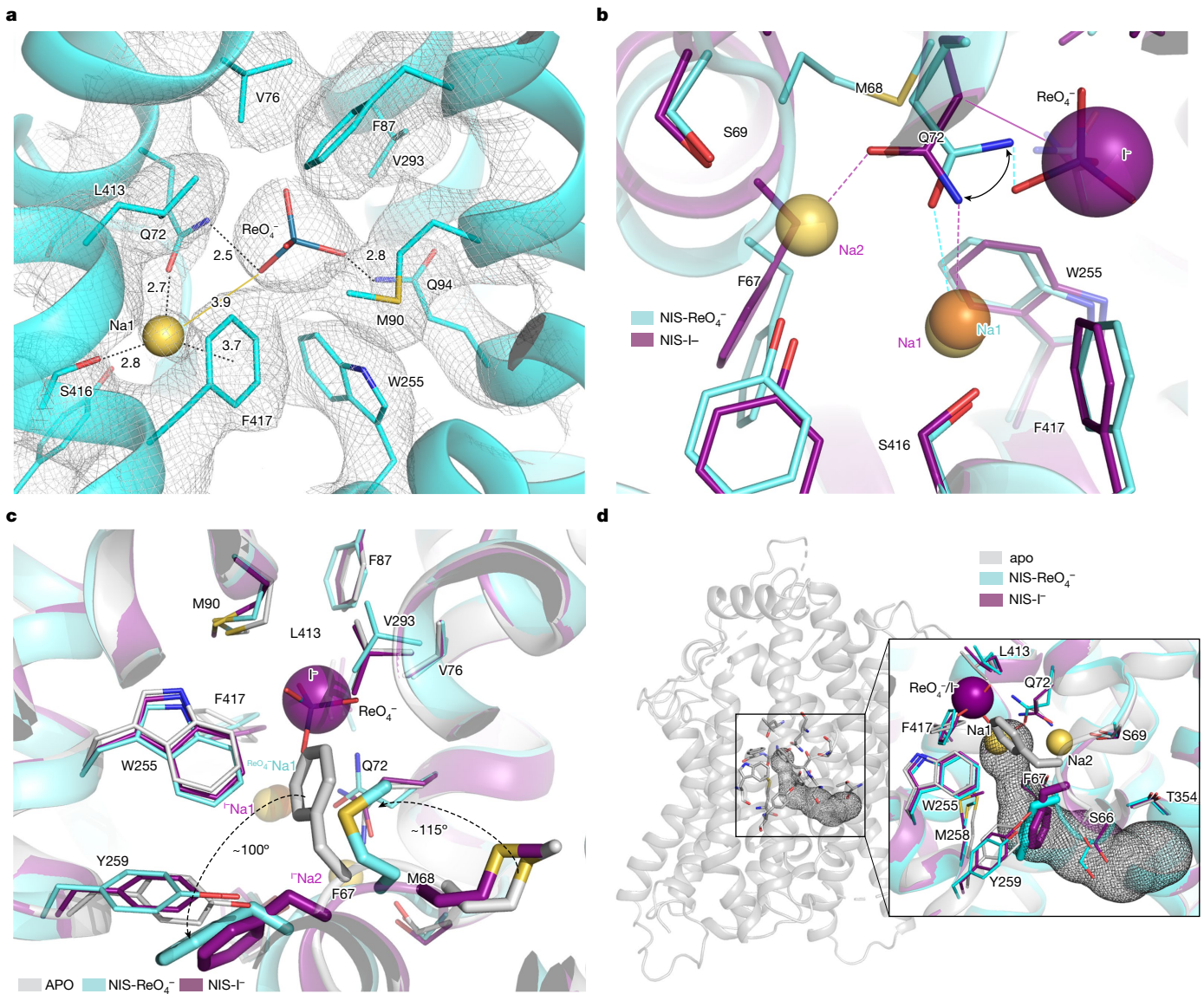


**Fig. 3 | Perrhenate-binding pocket and localized changes caused by ion binding.** **a**, Close-up of the  $\text{ReO}_4^-$ -binding pocket.  $\text{ReO}_4^-$  is represented by sticks and  $\text{Na}^+$  by a yellow sphere. Distances from  $\text{ReO}_4^-$  and  $\text{Na}^+$  to surrounding residues (within 3.9 Å) are indicated, as is the distance from  $\text{ReO}_4^-$  to  $\text{Na}^+$ . **b**, Close-up of the structural alignment of  $\text{NIS}-\text{I}^-$  and  $\text{NIS}-\text{ReO}_4^-$  showing the shift of Q72. **c**, Close-up of the structural alignment between apo-NIS,  $\text{NIS}-\text{I}^-$  and  $\text{NIS}-\text{ReO}_4^-$ . Arrowheads represent the shift of F67 and M68 from the

position they occupy in the apo-NIS structure to that in the substrate-bound structures. In the apo-NIS structure, F67 partially occupies the anion site.

**d**, Contour mesh of the tunnel calculated by Caver-Analyst in the apo-NIS structure that connects the substrate-binding pocket with the cytosol. Inset, alignment of the three structures showing that, in the substrate-bound NIS, F67 blocks the pathway from the binding sites to the cytosol.

experimentally by a density connecting the cation to F417, and  $\text{Na}^+$  to S69, Q72 and Y144 (Fig. 2c). Unlike the cations, however,  $\text{I}^-$  does not participate in intermolecular bonds with NIS and its exit route appears to be blocked by the cations. To simulate the accessible conformations of relevant residues in NIS with ions bound to it, we restrained only those cations with intermolecular (protein–ion) pseudobonds to the interacting protein residues, restraining them in particular positions using a harmonic potential.

A pathway analysis carried out on 1,059 snapshots sampled every 5 ns showed a tunnel similar to that in the apo-NIS structure in  $95 \pm 0.03\%$  of the snapshots. This suggests that the tunnel corresponds to a substrate-release pathway and that the  $\text{NIS}-\text{I}^-$  structure is in an occluded conformation (Fig. 3d) but is poised to open up into the cytosol (Supplementary Figs. 4 and 7b–e). Cation restraint was sufficient for the  $\text{I}^-$  to remain bound for an aggregated sampling time of 5 μs, suggesting that the cations are released before  $\text{I}^-$ .

Both F87 and L413 are at the ceiling of the binding cavity (Fig. 2b), and Q414 (which is flexible and hydrophilic) is just above it. These residues visited a number of conformers during the molecular dynamics simulations (Extended Data Fig. 8). The side chains of the conformers swing by up to 100°, allowing the ions to enter the symporter from the extracellular milieu. In molecular dynamics simulations with  $\text{NIS}-\text{I}^-$ , F67 fluctuates between conformations that open up the ion pocket to the exit path and those that interact with the anion (Supplementary Fig. 8). The latter interactions may help the ions exit.

## Discussion

In view of the above results, we propose that the structures we obtained are those boxed in Fig. 4a,b. We have shown—on the basis of state occupancies derived from kinetic data from whole cells expressing NIS endogenously, as analysed by statistical thermodynamics<sup>27</sup>—that, at

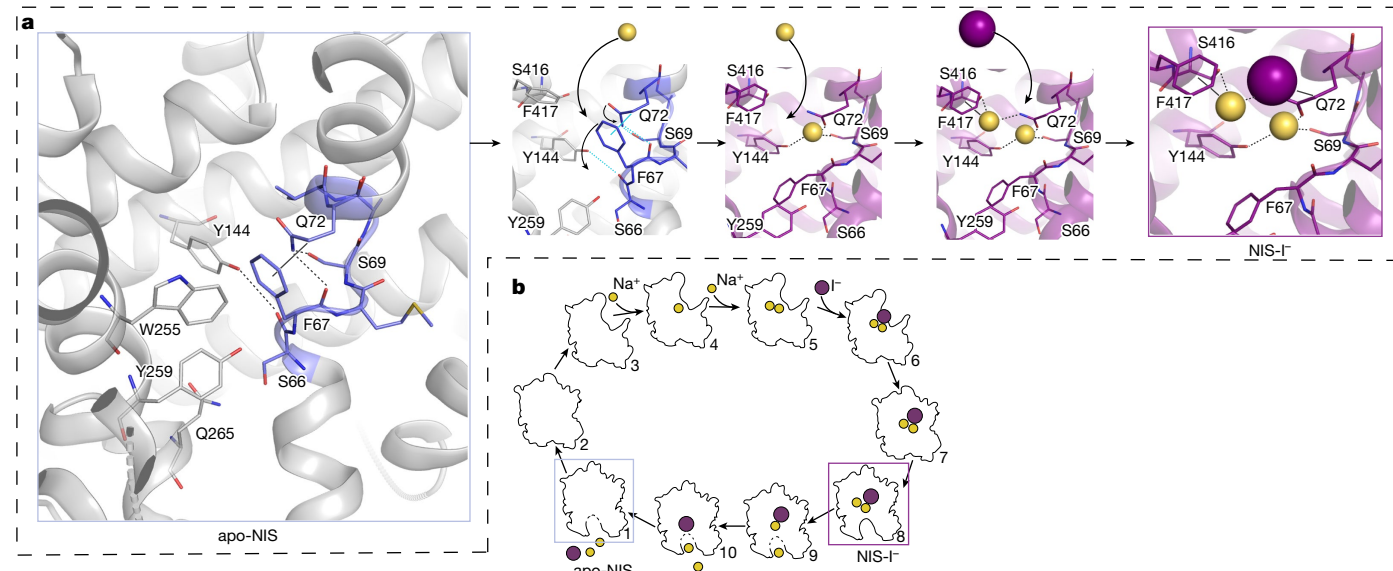


**Fig. 4 | NIS mechanism.** **a**, Left, mechanism of NIS substrate binding, starting from the apo-NIS structure. Right, a hydrogen bond network between F67, S69, Q72 and Y144 and a hydrophobic stacking interaction between F67 and Q72 are

disrupted by the binding of the first  $\text{Na}^+$ . This facilitates the binding of a second  $\text{Na}^+$  and subsequently of  $\text{I}^-$ . **b**, Cartoon of the putative NIS transport cycle. The experimental structures are enclosed in grey and magenta boxes.

physiological concentrations of  $\text{Na}^+$ , 79% of NIS molecules have two  $\text{Na}^+$  ions bound to them, which increases the affinity of NIS for  $\text{I}^-$  by a factor of ten (Fig. 4b, panels 5, 6). In these whole cells, of course, both the  $\text{Na}^+$  electrochemical gradient and membrane potential are present physiologically when the protein is at the plasma membrane. We hypothesize that the ternary complex isomerizes, causing NIS to adopt an occluded conformation that poises it to open up into the cytoplasm and release its substrates (Fig. 4b, panels 7–1), and that the unloaded symporter isomerizes to bind ions from the extracellular milieu and begin the next transport cycle (Fig. 4b, panels 2–4). The transport cycle of NIS, then, includes minimally the steps just described. The reason we did not capture the outwardly open conformation (Fig. 4b, panel 5) when  $\text{Na}^+$  was present and  $\text{I}^-$  absent is most probably that the NIS protein we used to determine the structure was solubilized in detergent and embedded in the detergent micelle: under these conditions, neither the  $\text{Na}^+$  electrochemical gradient nor the membrane potential is present.

An essential part of the mechanism of NIS is the coupling of  $\text{Na}^+$  transport to that of  $\text{I}^-$ . The NIS structures reported here show that, when  $\text{Na}^+$  binds to the  $\text{Na}_2$  site, it disrupts the hydrogen bond network that stabilizes the TMS2 kink in the apo-NIS structure (Fig. 4a), causing a conformational change that pushes F67 away from the anion-binding site (Fig. 3c,d) and thereby increasing the affinity of NIS for  $\text{Na}^+$  at the  $\text{Na}_1$  site and for  $\text{I}^-$ . In the NIS- $\text{ReO}_4^-$  structure the oxyanion interacts with Q72, moving it away from the  $\text{Na}_2$  site and thereby preventing it from coordinating  $\text{Na}^+$  at this site. In both  $\text{I}^-$  and oxyanion transport, the binding of  $\text{Na}^+$  at the  $\text{Na}_2$  site can trigger the structural change that enables the anion to bind (Extended Data Fig. 9). An alternative mechanism in which anion binding drives conformational changes seems unlikely, given that NIS has a low affinity for the anion in the absence of  $\text{Na}^+$  (ref. <sup>27</sup>).

How does NIS manage to stabilize so many ions in such close proximity to one another in the NIS- $\text{I}^-$  structure? One possible answer is that the cation reduces the  $\text{pK}_a$  of Q72, deprotonating the amino group and generating a negative charge at the carbonyl of the amide group, thus compensating for the positive charge of  $\text{Na}^+$  at the  $\text{Na}_2$  site and helping to bind  $\text{Na}^+$  at the  $\text{Na}_1$  site, with the electron pair remaining in the amide. Because  $\text{I}^-$  is an extremely weak base, the base required for the proposed electron rearrangement might be provided by solvent—that is, water molecules (or  $\text{OH}^-$ ) that may access the cation sites from the cytosolic side.

One of the most notable attributes of NIS is its ability to transport  $\text{I}^-$ , a very scarce ion, at the submicromolar concentrations at which it is found

in the extracellular milieu, because it is difficult to bind a halide ion such as  $\text{I}^-$  with high affinity. There remains, however, a very intriguing open question: why is the affinity of NIS for  $\text{I}^-$  so high? The answer lies in the special properties of  $\text{I}^-$ . As a  $4\text{d}^{10}\text{S}^2\text{P}^6$  moiety (identical to xenon),  $\text{I}^-$  is surrounded by a large unreactive electron cloud that endows it with unique properties that have been elucidated in previous computational studies. Sun et al.<sup>37</sup> investigated the behaviour of  $\text{Na}^+$  halides in a system with a water/air interface and found that  $\text{I}^-$  behaves differently to the other halides: not only does it show the highest number density close to the interface, but also its radial distribution ( $\rho(r)$ ) has its maximum several ångströms closer to the water/air interface than those of the other halides. These observations strongly suggest that, given the opportunity,  $\text{I}^-$  will interact with a hydrophobic environment. In agreement with this conclusion is our experimental evidence that most of the residues surrounding  $\text{I}^-$  are hydrophobic, and replacing them with polar residues affects NIS activity (Fig. 2b,d–e and Extended Data Fig. 5). Furthermore, the ability of NIS to discriminate so exquisitely between  $\text{Cl}^-$  and  $\text{I}^-$  seems to be due to both the size and the hydrophobicity of  $\text{I}^-$  (refs. <sup>38–40</sup>).

The fact that nature conserved the same structural fold across proteins that transport chemically diverse substrates may indicate that thousands of years of evolution have optimized a way to harness the energy stored in the  $\text{Na}^+$  electrochemical gradient to transport hydrophilic substrates against their concentration or electrochemical gradients—across the hydrophobic environment of the plasma membrane. So far, the prevailing expectation about a wide variety of mammalian transporters (SERT<sup>20</sup>, NKCC1 (ref. <sup>19</sup>), SGLT1 (ref. <sup>21</sup>), SGLT2 (ref. <sup>22</sup>), SMCT<sup>21</sup> and so on) has been that the location of their  $\text{Na}_2$ -binding site will correspond to that of the well-known canonical  $\text{Na}_2$ -binding site in the LeuT structure. This was indeed the case in SERT<sup>20,41,42</sup>, a member of the SLC6 family, although it is the only structure of a mammalian transporter in any of whose structures  $\text{Na}^+$  has been observed.

The structure of NIS with  $\text{Na}^+$  ions bound that we report here is, to our knowledge, the first structure of a member of the SLC5 family in which bound  $\text{Na}^+$  ions have been visualized. The  $\text{Na}^+$  ions bound to NIS are in the ion-binding cavity (Figs. 2c and 3b). The canonical hydroxyl group-containing residues (S353 and T354) do not show any densities attributable to  $\text{Na}^+$  ions (Supplementary Fig. 11). Although we have shown that S353 and T354 are important for NIS function<sup>18,36,43</sup>, they are in the exit pathway and not in the binding pocket. In fact, the first time it became clear at the molecular level that a patient had congenital

hypothyroidism due to a mutation in NIS, the mutation was precisely at position 354 (ref. <sup>43</sup>), and our characterization of the molecular requirements at this position led us to propose that NIS had the same fold as LeuT<sup>23</sup>. The fact that the Na<sub>2</sub> site in NIS is not the canonical site is not entirely surprising, given the marked difference between I<sup>-</sup> and leucine or serotonin, but it does defy the expectation that the Na<sub>2</sub> site should correspond to the canonical site in LeuT. Therefore, it will be of great interest to determine whether Na<sup>+</sup> ions bind to other members of the SLC5 family and to transporters in other families at the same site as they do in NIS, at other sites or at the LeuT canonical site. The members of the SLC5 family, in particular, transport carbohydrates (glucose, galactose, myoinositol), organic cations (choline) and monocarboxylates (nicotinate, butyrate and so on); among all these substrates, I<sup>-</sup> is the only halide anion<sup>21,22</sup>. Although all these proteins have (or are predicted to have) the same fold, critical differences will probably be found when their structures are determined because they transport extremely different substrates. Alignment of the sequences of the members of the SLC5 family (Supplementary Fig. 9) shows that certain residues in NIS are unique. For example, Q72 interacts with all three substrates in the NIS-I structure but the equivalent residue is a His in the sugar transporters and an Ala in the choline transporter. Q72H NIS and Q72A NIS are inactive, highlighting the critical role played by Q72 in NIS function (Fig. 2d).

The sodium/iodide symporter is of great significance in the basic field of plasma membrane transporters and for translational applications, ranging from imaging studies to cancer treatment. In addition, NIS has become increasingly important as a reporter molecule in preclinical and clinical gene transfer studies, making it possible to monitor the delivery of therapeutic genes and oncolytic viruses<sup>2,8,9</sup>. There is consequently no question that the determination of the NIS structures reported here will have a profound impact. The structures have not only greatly deepened our understanding of the NIS mechanism and transport cycle, but also enabled us to elucidate the roles of certain specific amino acids mutated in patients with iodide transport defects in NIS function and targeting to the plasma membrane<sup>2,6</sup> (Extended Data Fig. 10). The results presented here will pave the way for future determinations of the structure of NIS in different conformations and NIS molecules with different substrate selectivities and different stoichiometries, which will probably be extremely valuable in gene transfer studies and thus broaden the range of clinical applications of NIS.

## Online content

Any methods, additional references, Nature Portfolio reporting summaries, source data, extended data, supplementary information, acknowledgements, peer review information; details of author contributions and competing interests; and statements of data and code availability are available at <https://doi.org/10.1038/s41586-022-05530-2>.

- Portulano, C., Paroder-Belenitsky, M. & Carrasco, N. The Na<sup>+</sup>/I<sup>-</sup> symporter (NIS): mechanism and medical impact. *Endocr. Rev.* **35**, 106–149 (2014).
- Ravera, S., Reyna-Neyra, A., Ferrandino, G., Amzel, L. M. & Carrasco, N. The sodium/iodide symporter (NIS): molecular physiology and preclinical and clinical applications. *Annu. Rev. Physiol.* **79**, 261–289 (2017).
- Dai, G., Levy, O. & Carrasco, N. Cloning and characterization of the thyroid iodide transporter. *Nature* **379**, 458–460 (1996).
- Muller, R., Liu, Y. Y. & Brent, G. A. Thyroid hormone regulation of metabolism. *Physiol. Rev.* **94**, 355–382 (2014).
- Zhang, Z., Liu, F. & Chen, J. Molecular structure of the ATP-bound, phosphorylated human CFTR. *Proc. Natl Acad. Sci. USA* **115**, 12757–12762 (2018).
- Reyna-Neyra, A. et al. The iodide transport defect-causing Y348D mutation in the Na<sup>+</sup>/I<sup>-</sup> symporter renders the protein intrinsically inactive and impairs its targeting to the plasma membrane. *Thyroid* **31**, 1272–1281 (2021).
- Tazebay, U. H. et al. The mammary gland iodide transporter is expressed during lactation and in breast cancer. *Nat. Med.* **6**, 871–878 (2000).
- Spitzweg, C. et al. The sodium iodide symporter (NIS): novel applications for radionuclide imaging and treatment. *Endocr. Relat. Cancer* **28**, T193–T213 (2021).
- Kitzberger, C. et al. The sodium iodide symporter (NIS) as theranostic gene: its emerging role in new imaging modalities and non-viral gene therapy. *EJNMMI Res.* **12**, 25 (2022).
- Urnauer, S. et al. EGFR-targeted nonviral NIS gene transfer for bioimaging and therapy of disseminated colon cancer metastases. *Oncotarget* **8**, 92195–92208 (2017).
- Miller, A. & Russell, S. J. The use of the NIS reporter gene for optimizing oncolytic virotherapy. *Expert Opin. Biol. Ther.* **16**, 15–32 (2016).
- Li, W., Nicola, J. P., Amzel, L. M. & Carrasco, N. Asn441 plays a key role in folding and function of the Na<sup>+</sup>/I<sup>-</sup> symporter (NIS). *FASEB J.* **27**, 3229–3238 (2013).
- Nicola, J. P. et al. Sodium/iodide symporter mutant V270E causes stunted growth but no cognitive deficiency. *J. Clin. Endocrinol. Metab.* **100**, E1353–E1361 (2015).
- Paroder-Belenitsky, M. et al. Mechanism of anion selectivity and stoichiometry of the Na<sup>+</sup>/I<sup>-</sup> symporter (NIS). *Proc. Natl Acad. Sci. USA* **108**, 17933–17938 (2011).
- Levy, O. et al. N-linked glycosylation of the thyroid Na<sup>+</sup>/I<sup>-</sup> symporter (NIS). Implications for its secondary structure model. *J. Biol. Chem.* **273**, 22657–22663 (1998).
- Levy, O. et al. Characterization of the thyroid Na<sup>+</sup>/I<sup>-</sup> symporter with an anti-COOH terminus antibody. *Proc. Natl Acad. Sci. USA* **94**, 5568–5573 (1997).
- Paroder, V., Nicola, J. P., Ginter, C. S. & Carrasco, N. The iodide transport defect-causing mutation R124H: a δ-amino group at position 124 is critical for maturation and trafficking of the Na<sup>+</sup>/I<sup>-</sup> symporter (NIS). *J. Cell Sci.* **126**, 3305–3313 (2013).
- De la Vieja, A., Reed, M. D., Ginter, C. S. & Carrasco, N. Amino acid residues in transmembrane segment IX of the Na<sup>+</sup>/I<sup>-</sup> symporter play a role in its Na<sup>+</sup> dependence and are critical for transport activity. *J. Biol. Chem.* **282**, 25290–25298 (2007).
- Chew, T. A. et al. Structure and mechanism of the cation-chloride cotransporter NKCC1. *Nature* **572**, 488–492 (2019).
- Coleman, J. A., Green, E. M. & Gouaux, E. X-ray structures and mechanism of the human serotonin transporter. *Nature* **532**, 334–339 (2016).
- Han, L. et al. Structure and mechanism of the SGLT family of glucose transporters. *Nature* **601**, 274–279 (2022).
- Niu, Y. et al. Structural basis of inhibition of the human SGLT2-MAP17 glucose transporter. *Nature* **601**, 280–284 (2021).
- Yamashita, A., Singh, S. K., Kawate, T., Jin, Y. & Gouaux, E. Crystal structure of a bacterial homologue of Na<sup>+</sup>/Cl<sup>-</sup>-dependent neurotransmitter transporters. *Nature* **437**, 215–223 (2005).
- Faham, S. et al. The crystal structure of a sodium galactose transporter reveals mechanistic insights into Na<sup>+</sup>/sugar symport. *Science* **321**, 810–814 (2008).
- Wang, J., Liu, Z., Frank, J. & Moore, P. B. Identification of ions in experimental electrostatic potential maps. *IUCrJ* **5**, 375–381 (2018).
- Zhekova, H. R. et al. Mapping of ion and substrate binding sites in human sodium iodide symporter (hNIS). *J. Chem. Inf. Model.* **60**, 1652–1665 (2020).
- Nicola, J. P., Carrasco, N. & Amzel, L. M. Physiological sodium concentrations enhance the iodide affinity of the Na<sup>+</sup>/I<sup>-</sup> symporter. *Nat. Commun.* **5**, 3948 (2014).
- Ravera, S., Quick, M., Nicola, J. P., Carrasco, N. & Amzel, L. M. Beyond non-integer Hill coefficients: a novel approach to analyzing binding data, applied to Na<sup>+</sup>-driven transporters. *J. Gen. Physiol.* **145**, 555–563 (2015).
- Dohan, O. et al. The Na<sup>+</sup>/I<sup>-</sup> symporter (NIS) mediates electroneutral active transport of the environmental pollutant perchlorate. *Proc. Natl Acad. Sci. USA* **104**, 20250–20255 (2007).
- Tran, N. et al. Thyroid-stimulating hormone increases active transport of perchlorate into thyroid cells. *Am. J. Physiol. Endocrinol. Metab.* **294**, E802–E806 (2008).
- Zuckier, L. S. et al. Kinetics of perchlorate uptake and comparative biodistribution of perchlorate, pertechnetate, and iodide by Nal symporter-expressing tissues *in vivo*. *J. Nucl. Med.* **45**, 500–507 (2004).
- Eskandari, S. et al. Thyroid Na<sup>+</sup>/I<sup>-</sup> symporter. Mechanism, stoichiometry, and specificity. *J. Biol. Chem.* **272**, 27230–27238 (1997).
- Llorente-Esteban, A. et al. Allosteric regulation of mammalian Na<sup>+</sup>/I<sup>-</sup> symporter activity by perchlorate. *Nat. Struct. Mol. Biol.* **27**, 533–539 (2020).
- Boutagy, N. E. et al. Noninvasive *in vivo* quantification of adeno-associated virus serotype 9-mediated expression of the sodium/iodide symporter under hindlimb ischemia and neuraminidase desialylation in skeletal muscle using single-photon emission computed tomography/computed tomography. *Circ. Cardiovasc. Imaging* **12**, e009063 (2019).
- Pavelka, A. et al. CAVER: algorithms for analyzing dynamics of tunnels in macromolecules. *IEEE/ACM Trans. Comput. Biol. Bioinform.* **13**, 505–517 (2016).
- Ferrandino, G. et al. Na<sup>+</sup> coordination at the Na<sub>2</sub> site of the Na<sup>+</sup>/I<sup>-</sup> symporter. *Proc. Natl Acad. Sci. USA* **113**, E5379–E5388 (2016).
- Sun, L. et al. Molecular dynamics simulations of the surface tension and structure of salt solutions and clusters. *J. Phys. Chem.* **116**, 3198–3204 (2012).
- Carugo, O. Buried chloride stereochemistry in the Protein Data Bank. *BMC Struct. Biol.* **14**, 19 (2014).
- Kang, B., Tang, H., Zhao, Z. & Song, S. Hofmeister series: insights of ion specificity from amphiphilic assembly and interface property. *ACS Omega* **5**, 6229–6239 (2020).
- Marcus, Y. A simple empirical model describing the thermodynamics of hydration of ions of widely varying charges, sizes, and shapes. *Biophys. Chem.* **51**, 111–127 (1994).
- Yang, D. & Gouaux, E. Illumination of serotonin transporter mechanism and role of the allosteric site. *Sci. Adv.* **7**, eabl3857 (2021).
- Coleman, J. A. & Gouaux, E. Structural basis for recognition of diverse antidepressants by the human serotonin transporter. *Nat. Struct. Mol. Biol.* **25**, 170–175 (2018).
- Levy, O., Ginter, C. S., De la Vieja, A., Levy, D. & Carrasco, N. Identification of a structural requirement for thyroid Na<sup>+</sup>/I<sup>-</sup> symporter (NIS) function from analysis of a mutation that causes human congenital hypothyroidism. *FEBS Lett.* **429**, 36–40 (1998).

**Publisher's note** Springer Nature remains neutral with regard to jurisdictional claims in published maps and institutional affiliations.

Springer Nature or its licensor (e.g. a society or other partner) holds exclusive rights to this article under a publishing agreement with the author(s) or other rightsholder(s); author self-archiving of the accepted manuscript version of this article is solely governed by the terms of such publishing agreement and applicable law.

© The Author(s), under exclusive licence to Springer Nature Limited 2022

## Methods

### Cell culture

Cell lines COS-7, obtained from the American Type Culture Collection, and 293F, obtained from GIBCO, were cultured in DMEM medium (GIBCO) supplemented with 10% fetal bovine serum (GIBCO), 10 mM glutamine and 100 U ml<sup>-1</sup> penicillin/streptomycin (GIBCO). 293F cells in suspension were maintained in Free-Style Media (GIBCO) supplemented with 2% fetal bovine serum.

### Site-directed mutagenesis

Mutants F67, S69, Q72, M90, Q94, Y144, V293, S416 and F417 NIS were generated using as a template HA-tagged NIS cloned into pcDNA3.1. PCR was performed with primers carrying the relevant specific codon using Kod Hot Start DNA polymerase (Novagen). After digestion with DpnI (NEB) to eliminate parental DNA, the PCR product was transformed into XL1 Blue Supercompetent *Escherichia coli*. All constructs were sequenced to verify the specific nucleotide substitutions that had been made.

### Flow cytometry

Paraformaldehyde-fixed cells were incubated with 0.1 µg ml<sup>-1</sup> anti-HA (YPYDVPDYA) antibody (Roche Applied Science) in PBS/BSA (0.2%) followed by 50 nM PE-conjugated goat anti-rat antibody (Life Technologies). The fluorescence of 50,000 cells per sample was assayed with a FACSCalibur flow cytometer (BD Biosciences). Data were analysed using FlowJo software (Tree Star)<sup>44</sup>.

### Whole-cell iodide transport

Cells were transiently transfected in 10 cm plates using either 4 µg of HA-tagged NIS in pcDNA3.1 and Lipofectamine/Plus reagent (Life Technologies) or 25 µg of cDNAs and PEI MAX (Polyscience). After 24 h these were split into 24-well/plates and after 48 h were washed twice with HBSS (140 mM NaCl, 5.4 mM KCl, 1.3 mM CaCl<sub>2</sub>, 0.4 mM MgSO<sub>4</sub>, 0.5 mM MgCl<sub>2</sub>, 0.4 mM Na<sub>2</sub>HPO<sub>4</sub>, 0.44 mM KH<sub>2</sub>PO<sub>4</sub>, 5.55 mM glucose and 10 mM HEPES, pH 7.4) following a previously published protocol<sup>44</sup>. For steady-state experiments, cells were incubated with HBSS containing 10, 20, 100 or 200 µM KI supplemented with carrier-free <sup>125</sup>I at a specific activity of 50 µCi µmol<sup>-1</sup>, at 37 °C for 45 min in a CO<sub>2</sub> incubator. For I<sup>-</sup>-dependent kinetic analysis, cells were incubated in HBSS buffer containing the I<sup>-</sup> concentrations indicated (1.2–600 µM) for 2 min. Cells were then washed with HBSS, lysed with ice-cold ethanol and intracellular <sup>125</sup>I was quantitated using a Cobra III Gamma Counter (Perkin Elmer). Kinetic parameters were determined by Michaelis–Menten or Hill equation linear regression after subtraction of the background recorded in cells transfected with a NIS-free plasmid, and were analysed using Origin 2021 and GraphPad Prism 9.4.

### Protein overexpression and purification

Transduction of 293F cells was performed with a lentiviral vector containing a rat NIS cDNA construct with a HA tag at the N terminus and a His8 tag and streptavidin-binding protein (IBA) tag at the C terminus, and these were enriched for positive cells by flow cytometry with a HA tag. Up to 97% of positive cells were then grown in suspension<sup>45</sup>.

At a density of 2.5 × 10<sup>6</sup> ml<sup>-1</sup>, 293F cells were collected and resuspended in a buffer containing 75 mM Tris-HCl pH 8.0, 350 mM NaCl and protease inhibitor cocktail (Roche) and disrupted using an Emulsiflex C3 homogenizer (Avestin). Cell debris was removed by centrifugation at 10,000g for 10 min, and the membrane-containing supernatant was collected and subjected to ultraspeed centrifugation at 250,000g for 3 h. Membranes were resuspended in the extraction buffer containing 75 mM Tris-HCl (pH 8.0), 350 mM NaCl and protease inhibitor cocktail (Roche) and incubated with 0.5% lauryl maltose neopentyl

glycol (LMNG) and 0.5% glyco-diosgenin (GDN) for 2 h at 4 °C. NIS was subsequently purified via Strep-Tactin affinity chromatography and size exclusion chromatography using Superdex 200 increase in the presence of 350 mM NaCl, 75 mM Tris-HCl pH 8.0 and 0.005% LMNG/GDN.

The fraction corresponding to the peak of the chromatogram was then used for EM preparation.

### Cryo-sample preparation

All cryo-EM grids were prepared by the application of 2.5 µl of protein at around 2 mg ml<sup>-1</sup> to freshly glow-discharged Quantifoil 1.2/1.3, 200 mesh (Electron Microscopy Sciences), blotted for 4–6 s at 100% humidity and 7 °C and plunge-frozen in liquid nitrogen-cooled liquid ethane using a Vitrobot Mark IV (Thermo Fisher Scientific).

### Data acquisition and processing

All cryo-EM datasets were collected using SerialEM software on a Titan Krios G2 (ThermoFisher) electron microscope (Yale University Cryo-EM Resource) operated at 300 kV and equipped with a GIF Quantum LS imaging filter (Gatan) and a K3 summit direct electron detector (Gatan). Images were acquired at a super-resolution pixel size of 0.534 Å. The dose rate was 16.1 e per physical pixel s<sup>-1</sup>, yielding a total dose of 45 e Å<sup>-2</sup>. Video stacks were drift-corrected using MotionCorr2 (ref. <sup>46</sup>) with a 5 × 5 patch and twofold binning. Contrast transfer function (CTF) information was estimated from dose-weighted images by CTFFind4.1 (ref. <sup>47</sup>).

Two datasets for NIS in the presence of its substrate Na<sup>+</sup> were acquired in two separate sessions from two different protein preparations, yielding 3,861 and 4,164 videos, respectively. Each dataset was analysed individually. Movie stacks were drift-corrected using MotionCorr2 (ref. <sup>46</sup>) with a 5 × 5 patch and twofold binning. CTF information was estimated from dose-weighted images by CTFFind4.1 (ref. <sup>47</sup>) in Relion<sup>48</sup> with exhaustive searching. Particles were picked by Relion Auto-picking using Laplacian-of-Gaussian blob detection. After extraction of particles at a size of 2.73 Å per pixel, three rounds of 2D classification were performed using the fast subset for a larger dataset followed by one with all data. After selection of good classes, contributing particles were re-extracted at the original size (1.068 Å per pixel), and multiple rounds of three-dimensional (3D) classification and 3D autorefinement were performed in Relion. The final particles leading to the best 3D-refined maps in both datasets were combined and subjected to additional 3D classification and 3D refinement. The final pool of 108,000 selected particles was extracted with different particle box sizes and imported in cryoSPARC<sup>49</sup>. Nonuniform refinement<sup>50</sup> of several particle sets led to the choice of optimal particle box size (288 pixels)<sup>51</sup>; subsequent global CTF refinement and nonuniform refinement resulted in a 3.47 Å map. The NIS model was built in Coot<sup>52</sup> and refined in Phenix<sup>53</sup> Real Space Refine. Local resolution analysis was performed in cryoSPARC. We used Chimera<sup>54</sup> to generate a mask around one of the monomers and cryoSPARC to locally refine the map, thereby obtaining the final 3.29 Å map. The model was then further refined in Phenix, yielding the final structure.

A dataset for NIS in the presence of both its substrates, Na<sup>+</sup> and I<sup>-</sup> (purification buffer supplemented with 2 mM KI), was acquired for a total of 3,867 videos. Particles were chosen by Relion Auto-picking using Laplacian-of-Gaussian blob detection for a total of 3 × 10<sup>6</sup> particles, followed by three rounds of 2D classification using the fast subset for a larger dataset and the final one with all the data. After class selection, particles were re-extracted at the original size (1.068 Å per pixel) and multiple rounds of 3D classification and 3D autorefine were performed in Relion 3.0.8. The final pool of particles was then re-extracted with a different box size and imported in cryoSPARC<sup>49</sup>. Nonuniform refinement<sup>50</sup> of several particle sets led to the choice of optimal particle box size (288 pixels)<sup>51</sup>; subsequent global CTF refinement and nonuniform refinement resulted in a 3.46 Å map.

The NIS model was built in Coot<sup>52</sup> and refined in Phenix<sup>53</sup> Real Space Refine. Local resolution analysis was performed in cryoSPARC using local resolution estimation, and density maps were prepared with UCSF Chimera<sup>54</sup>. We used Chimera to generate a mask around one of the monomers and cryoSPARC to locally refine the map, thereby obtaining the final 3.12 Å map. The model was then further refined in Phenix, yielding the final structure.

A dataset for NIS in the presence of both its substrates, Na<sup>+</sup> and ReO<sub>4</sub><sup>-</sup> (purification buffer supplemented with 1 mM NaReO<sub>4</sub>), was acquired, for a total of 4,431 videos. Particles were chosen by Relion Auto-picking using Laplacian-of-Gaussian blob detection for a total of  $3 \times 10^6$  particles, followed by three rounds of 2D classification using the fast subset for a larger dataset and the final one with all the data. After class selection, particles were re-extracted at the original size (1.068 Å per pixel) with a different box size and imported in cryoSPARC<sup>49</sup>. Several rounds of heterogeneous refinement led to a final total of 432,000 particles that were then subjected to nonuniform refinement<sup>50</sup> and subsequent global CTF refinement to obtain a 3.24 Å map. The NIS model was built in Coot<sup>52</sup> and refined in Phenix<sup>53</sup> Real Space Refine. Local resolution analysis was performed in cryoSPARC. Symmetry expansion and local refinement, applying a mask covering a single monomer, led to a map with 3.15 Å resolution. The NIS model was then refined in Phenix<sup>53</sup> Real Space Refine. Images of NIS maps and models were generated using Pymol (v.2) and Chimera (1.15).

## Ion identification

Because a cryo-EM density map reflects electrostatic potentials, we sought to quantitate density in the vicinity of the ion sites. We ascertained the I<sup>-</sup> and ReO<sub>4</sub><sup>-</sup> map densities along 24 lines (48 equally spaced directions generated using HealPix pixelation<sup>55</sup>) centred on each ion position. Densities along the lines were evaluated by trilinear interpolation on a four-times Fourier-upsampled density map using Matlab 2020a. An overall spherically averaged density (as a function of radial distance from the ion) was also computed from the upsampled map. To aid comparison of numerical values between maps, density values in each map were normalized using the peak density at the α-carbon positions of residues Q72 and Q94 (refs. <sup>55,56</sup>).

## Molecular dynamics simulations

Molecular dynamics simulations were carried out using the NIS-I-structure (Na<sup>+</sup>:I<sup>-</sup>, 2:1) embedded in a pre-equilibrated 1,2-dioleoyl-sn-glycero-3-phosphocholine bilayer. We obtained the parameters and scripts for the minimization, equilibration and production in GROMACS using CHARMM-GUI<sup>57</sup>. The composition of the system in the production runs is summarized in Supplementary Table 1. All simulations were carried out with GROMACS v.2020 (ref. <sup>58</sup>), in conjunction with the CHARMM36 force field<sup>59</sup>. Van der Waals interactions were cut off at 1 nm, and electrostatics were treated by PME<sup>60</sup> beyond 1 nm. Temperature and pressure were maintained at 310.5 K and 1 bar, respectively, using the V-Rscale thermostat<sup>61</sup> and Parrinello–Rahman barostat<sup>62</sup>, respectively. All bonds were restrained using LINCS<sup>63</sup>, and an integration time step of 2 fs was used. We energy minimized (steepest descent) using a double-precision version of GROMACS, and six steps (125, 125, 125, 500, 500 and 500 ns) of position restraint with a gradually increased harmonic force constant (Fc) with different values for backbone atoms (100,000, 2,000, 1,000, 500, 200 and 50 kJ mol<sup>-1</sup> nm<sup>-2</sup>), side-chain atoms (2,000, 2,000, 1,000, 500, 200, 50 and 0 kJ mol<sup>-1</sup> nm<sup>-2</sup>), residue dihedrals (1,000, 200, 200, 100 and 0 kJ mol<sup>-1</sup> nm<sup>-2</sup>) and lipids (1,000, 400, 400, 200, 40 and 0 kJ mol<sup>-1</sup> nm<sup>-2</sup>). Van der Waals parameters for I<sup>-</sup> were taken from Li et al.<sup>64</sup>.

## Reporting summary

Further information on research design is available in the Nature Portfolio Reporting Summary linked to this article.

## Data availability

Cryo-EM maps and atomic coordinates of the structures presented in this manuscript have been deposited in the Protein Data Bank (PDB) and Electron Microscopy Data Bank (EMDB) under accession codes 7UUY and EMD-26806 (for Apo-NIS), 7UV0 and EMD-26808 (for NIS-I<sup>-</sup>) and 7UUZ and EMD-26807 (for NIS-ReO<sub>4</sub><sup>-</sup>). The trajectories and the Jupyter notebook used for molecular dynamics simulations are available at <https://codeocean.com/capsule/1458259/tree>.

44. Ferrandino, G. et al. Na<sup>+</sup> coordination at the Na2 site of the Na<sup>+</sup>/I<sup>-</sup> symporter. *Proc. Natl Acad. Sci. USA* **113**, E5379–E5388 (2016).
45. Ravera, S., Quick, M., Nicola, J. P., Carrasco, N. & Amzel, L. M. Beyond non-integer Hill coefficients: a novel approach to analyzing binding data, applied to Na<sup>+</sup>-driven transporters. *J. Gen. Physiol.* **145**, 555–563 (2015).
46. Zheng, S. Q. et al. MotionCor2: anisotropic correction of beam-induced motion for improved cryo-electron microscopy. *Nat. Methods* **14**, 331–332 (2017).
47. Rohou, A. & Grigorieff, N. CTFFIND4: fast and accurate defocus estimation from electron micrographs. *J. Struct. Biol.* **192**, 216–221 (2015).
48. Scheres, S. H. RELION: implementation of a Bayesian approach to cryo-EM structure determination. *J. Struct. Biol.* **180**, 519–530 (2012).
49. Punjani, A., Rubinstein, J. L., Fleet, D. J. & Brubaker, M. A. cryoSPARC: algorithms for rapid unsupervised cryo-EM structure determination. *Nat. Methods* **14**, 290–296 (2017).
50. Punjani, A., Zhang, H. & Fleet, D. J. Non-uniform refinement: adaptive regularization improves single-particle cryo-EM reconstruction. *Nat. Methods* **17**, 1214–1221 (2020).
51. Moriya, T. et al. Size matters: optimal mask diameter and box size for single-particle cryogenic electron microscopy. Preprint at bioRxiv <https://doi.org/10.1101/2020.08.23.263707> (2020).
52. Emsley, P. & Cowtan, K. Coot: model-building tools for molecular graphics. *Acta Crystallogr. D* **60**, 2126–2132 (2004).
53. Adams, P. D. et al. PHENIX: a comprehensive Python-based system for macromolecular structure solution. *Acta Crystallogr. D* **66**, 213–221 (2010).
54. Pettersen, E. F. et al. UCSF Chimera—a visualization system for exploratory research and analysis. *J. Comput. Chem.* **25**, 1605–1612 (2004).
55. Górski, K. M. et al. HEALPix: a framework for high-resolution discretization and fast analysis of data distributed on the sphere. *Astrophys. J.* **622**, 759–771 (2005).
56. Wang, J., Liu, Z., Frank, J. & Moore, P. B. Identification of ions in experimental electrostatic potential maps. *IUCrJ* **5**, 375–381 (2018).
57. Lee, J. et al. CHARMM-GUI input generator for NAMD, GROMACS, AMBER, OpenMM, and CHARMM/OpenMM simulations using the CHARMM36 additive force field. *J. Chem. Theory Comput.* **12**, 405–413 (2016).
58. Abraham, M. J. et al. GROMACS: high performance molecular simulations through multi-level parallelism from laptops to supercomputers. *SoftwareX* **1**, 19–25 (2015).
59. Huang, J. et al. CHARMM36m: an improved force field for folded and intrinsically disordered proteins. *Nat. Methods* **14**, 71–73 (2017).
60. Essmann, U. et al. A smooth particle mesh Ewald method. *J. Chem. Phys.* **103**, 8577–8593 (1995).
61. Bussi, G., Donadio, D. & Parrinello, M. Canonical sampling through velocity rescaling. *J. Chem. Phys.* **126**, 014101 (2007).
62. Parrinello, M. & Rahman, A. Polymorphic transitions in single crystals: a new molecular dynamics method. *J. Appl. Phys.* **52**, 7182–7190 (1981).
63. Hess, B., Bekker, H., Berendsen, H. J. & Fraaije, J. G. LINCS: a linear constraint solver for molecular simulations. *J. Comput. Chem.* **18**, 1463–1472 (1997).
64. Li, P., Song, L. F. & Merz, K. M. Jr. Systematic parameterization of monovalent ions employing the nonbonded model. *J. Chem. Theory Comput.* **11**, 1645–1657 (2015).

**Acknowledgements** We thank H. Mchaourab and members of the Carrasco laboratory for critical reading of the manuscript and insightful discussion, and S. Gabelli for helpful suggestions. This study was supported by National Institutes of Health (NIH) grants GM R01 114250 (to N.C. and L.M.A.), NS021501 (to F.J.S.) and NINDS R21NS108842, and a Pamela Mars Wright Innovator Award (to M.A.B.). We thank S. Wu of the Yale Cryo-EM Resource facility for screening and data collection. This work was conducted in part using the CPU and GPU resources at the Advanced Computing Center for Research and Education at Vanderbilt University and at the Maryland Advanced Research Computing Center. We used the DORS storage system supported by NIH (no. S1ORRO31634 to J. Smith).

**Author contributions** S.R., N.C. and L.M.A. conceived the project. S.R. expressed and purified proteins and prepared cryo-grids. S.R. and E.K. processed cryo-EM data. S.R., E.K., L.M.A. and M.A.B. built and refined the atomic models. F.J.S. implemented the protocol for ion identification. S.R. and M.A.B. carried out molecular dynamics simulations. S.R., J.P.N. and G.S.S. generated mutant NIS proteins and carried out functional assays. S.R. and N.C. wrote the manuscript with input from all authors.

**Competing interests** The authors declare no competing interests.

### Additional information

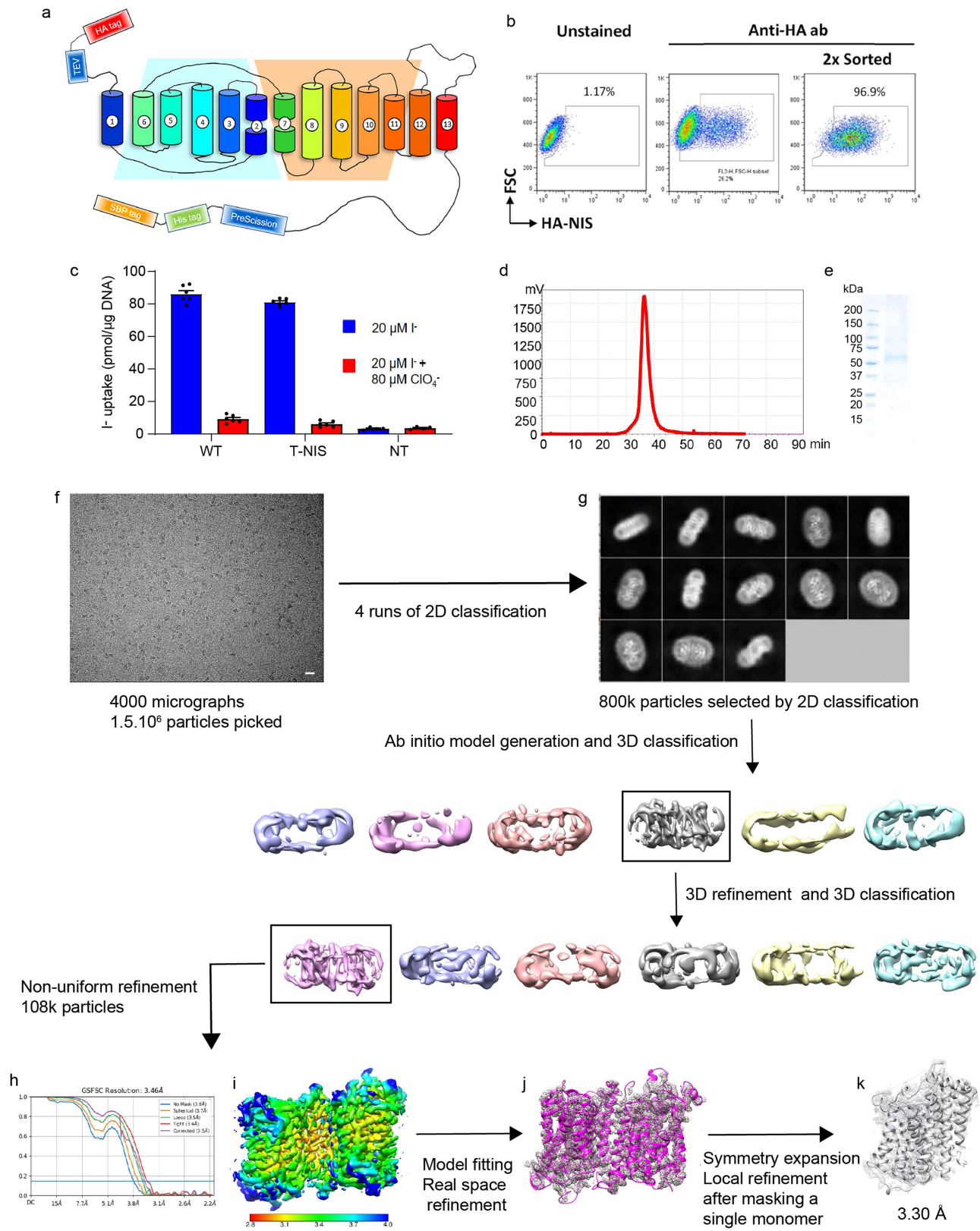
**Supplementary information** The online version contains supplementary material available at <https://doi.org/10.1038/s41586-022-05530-2>.

**Correspondence and requests for materials** should be addressed to Nancy Carrasco.

**Peer review information** *Nature* thanks Jue Chen, Wojciech Kopec, Christine Spitzweg and the other, anonymous, reviewer(s) for their contribution to the peer review of this work.

**Reprints and permissions information** is available at <http://www.nature.com/reprints>.

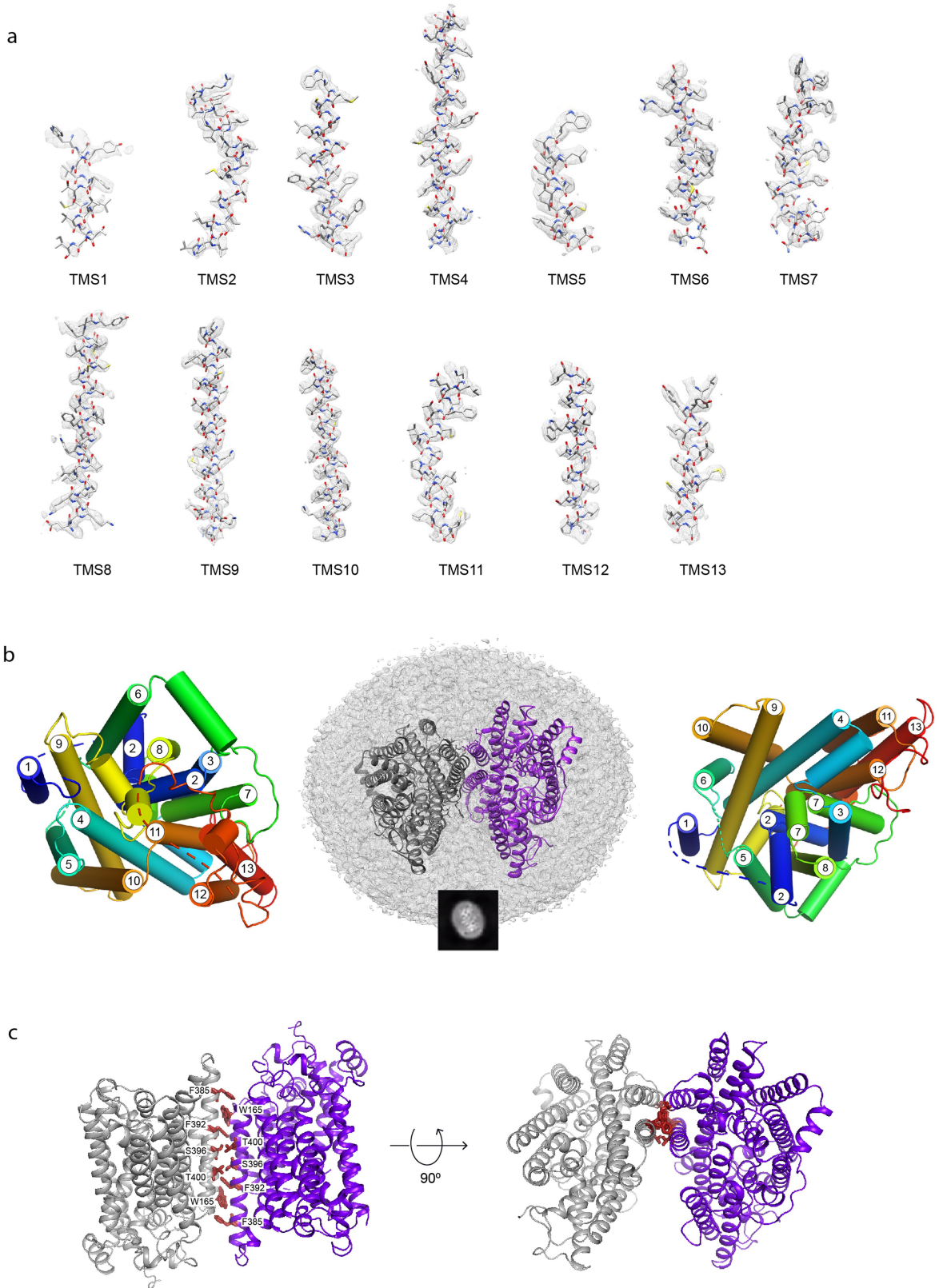
# Article



**Extended Data Fig. 1** | See next page for caption.

**Extended Data Fig. 1 | Cryo-EM data processing and determination of the structure of NIS.** Topology model of the engineered NIS molecule (T-NIS) whose cDNA was used to transduce 293F cells. We engineered an HA tag onto the N-terminus and a HIS and an SBP (streptavidin-binding protein) tag onto the C-terminus for affinity purification. The tags are separated from NIS by a TEV protease site at the N-terminus and a PreScission site at the C-terminus. **b.** Enrichment of 293F cells expressing NIS by flow cytometry using an anti-HA antibody. After two rounds of sorting, >96% of the cells expressed NIS at the plasma membrane. **c.** I<sup>-</sup> transport assay. T-NIS transports virtually as much I<sup>-</sup> as wild-type (WT) NIS does, whereas nontransduced (NT) cells transport no I<sup>-</sup>. Results are expressed as pmol of I<sup>-</sup> accumulated/μg DNA ± s.e.m. Values represent averages of the results from two different experiments, each of

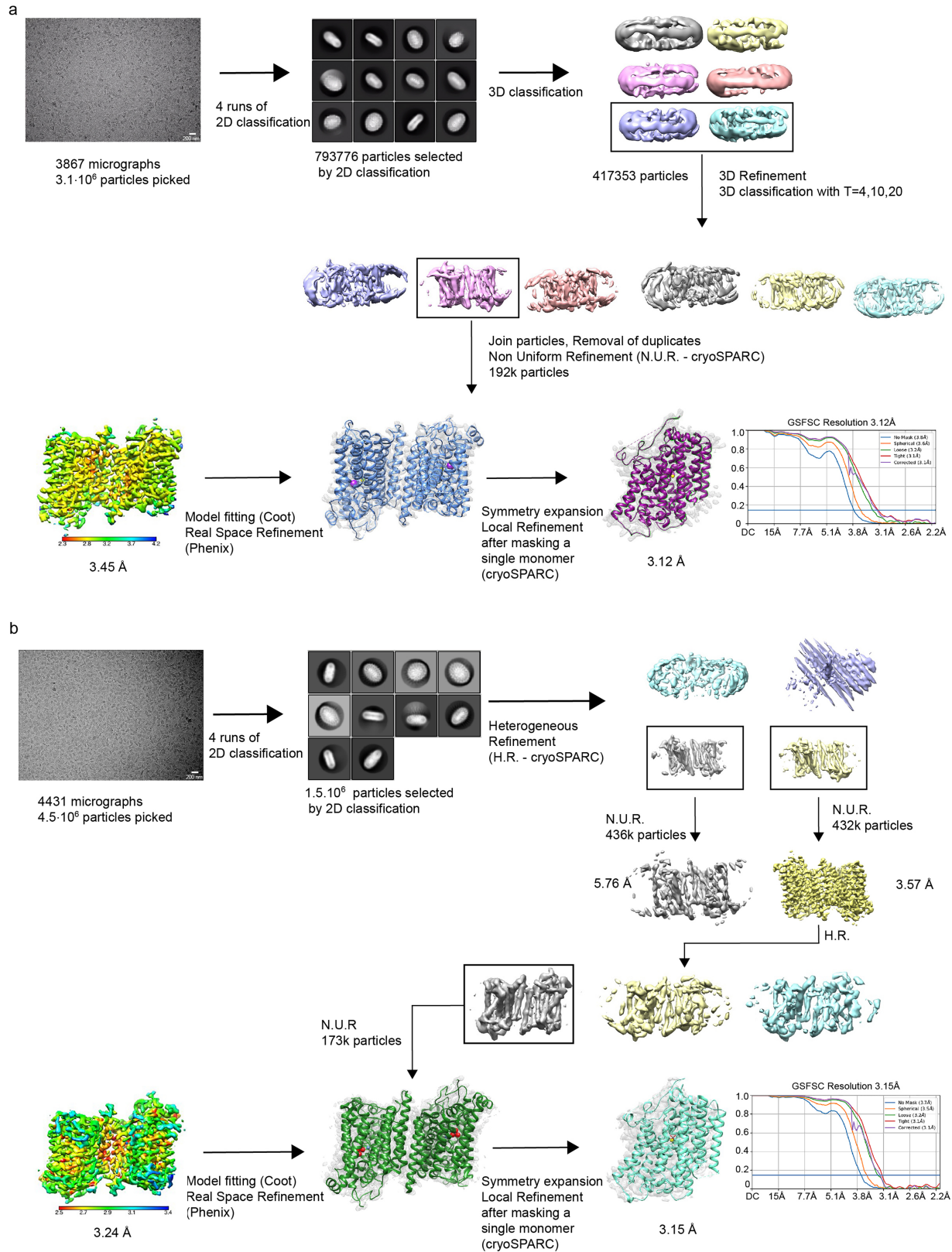
which was carried out in triplicate (n = 6). **d.** Size exclusion chromatography (SEC) of the fraction of NIS purified in LMNG/GDN used for cryo-EM imaging detected by Trp-fluorescence. **e.** Coomassie blue staining of SEC-purified NIS subjected to SDS-PAGE (representative gel (n=3); see also Supplementary Fig. 1). **f.** Cryo-EM micrograph of apo-NIS (representative of 8025 micrographs that yielded similar results). The scale bar represents 200 nm. **g.** Selected 2D class averages obtained after 4 rounds of 2D classification using Relion (top image) and data-processing workflow (bottom two rows). **h.** Fourier shell correlation (FSC) of the locally refined map. **i.** NIS dimer map colored according to local resolution. **j.** Fitting of NIS sequence to the electron density map. **k.** Local refinement.



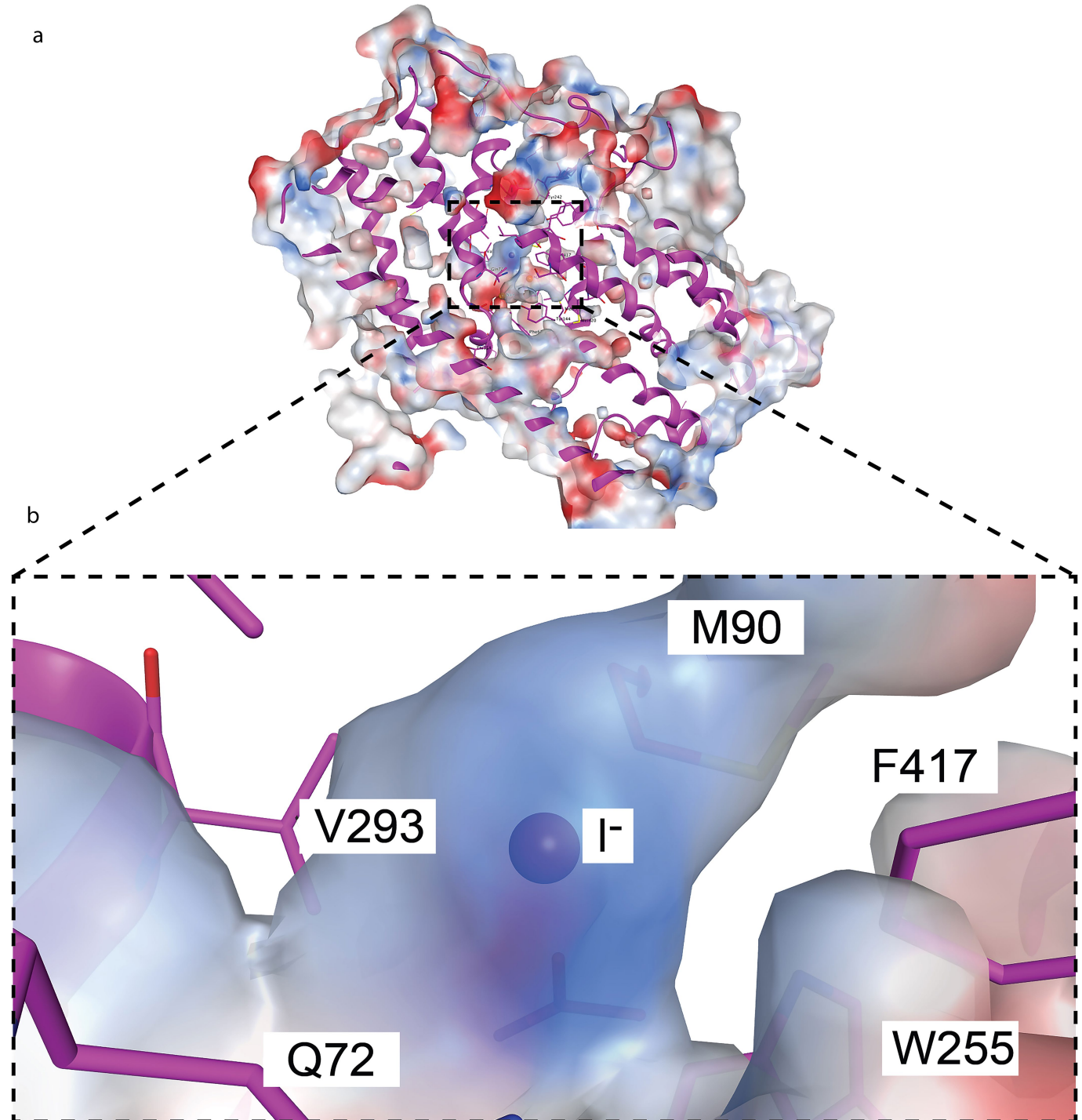
**Extended Data Fig. 2 | Cryo-EM densities and model of TMs and dimeric assembly of NIS.** **a.**  $\alpha$ -helical features are clearly visible in all 13 TMs.

**b.** NIS structure viewed from the extracellular side of the membrane, with the numbered TMs depicted as cylinders (left panel). NIS embedded in the

membrane, top view; an example of 2D classes representing the corresponding view is shown in the black square (middle panel). NIS structure viewed from the intracellular side of the membrane, with the numbered TMs depicted as cylinders (right panel). **c.** Residues interacting at the dimer interface in apo-NIS.



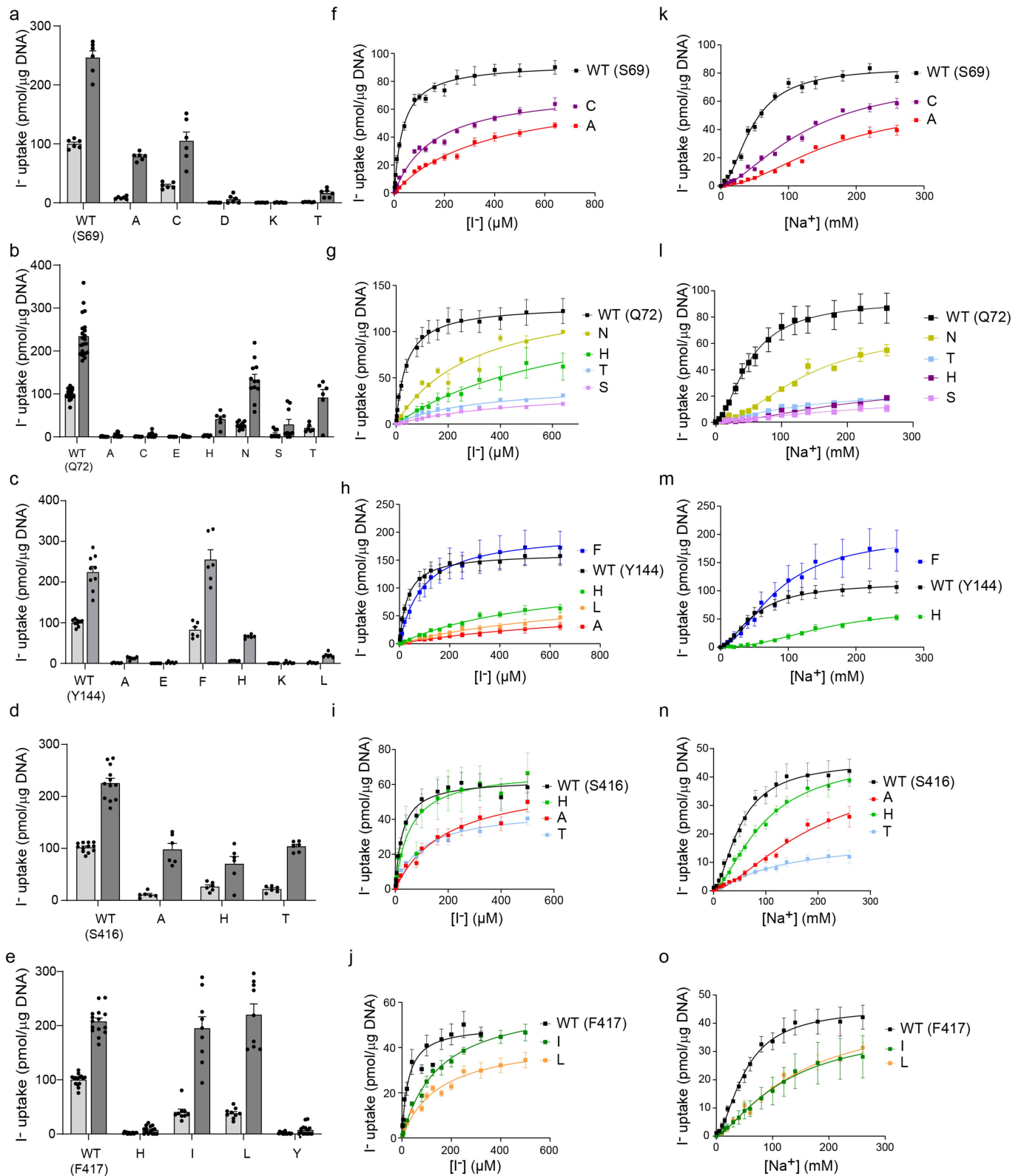
**Extended Data Fig. 3 | Cryo-EM data processing and determination of the structures of NIS with substrates bound. a. NIS-I-. b. NIS-ReO<sub>4</sub><sup>-</sup>.**


**Extended Data Fig. 4 |  $\text{I}^-$  binds to a partially positively charged cavity.**

**a.** NIS- $\text{I}^-$  side view. The solvent accessible surface is colored according to the electrostatic potential using a double gradient between  $-2 \text{ EV}$  (red) and  $0$  (white)

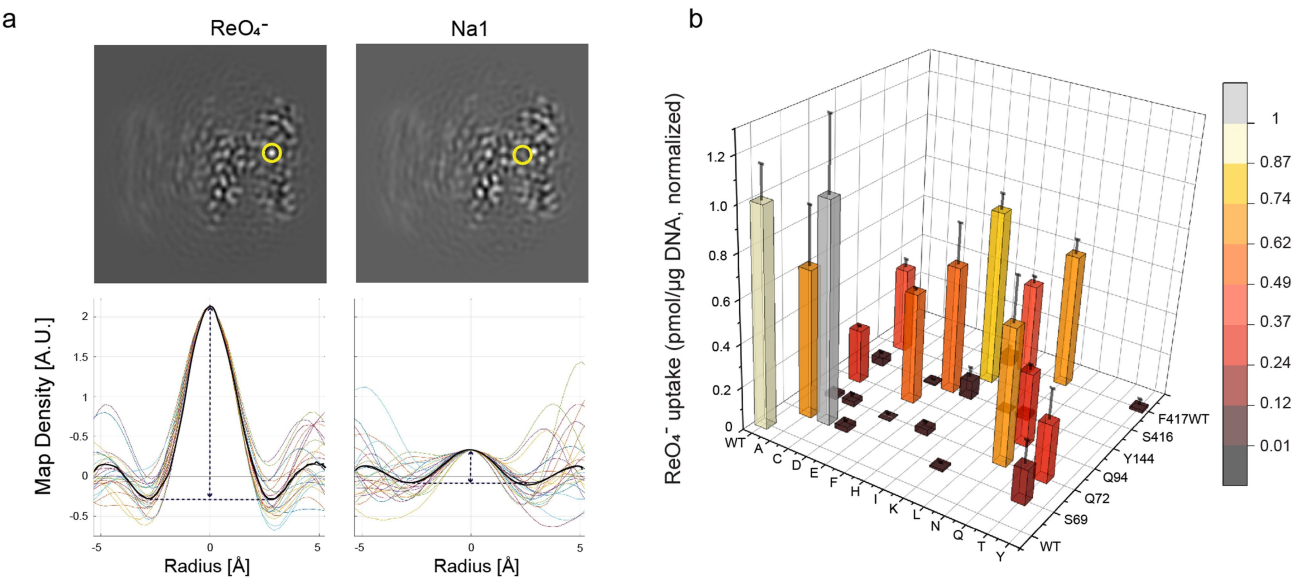
and between  $0$  and  $2 \text{ EV}$  (blue) and cropped to expose the  $\text{I}^-$  binding cavity.

**b.** Close-up of the  $\text{I}^-$  binding cavity showing the positive nature of its surface.



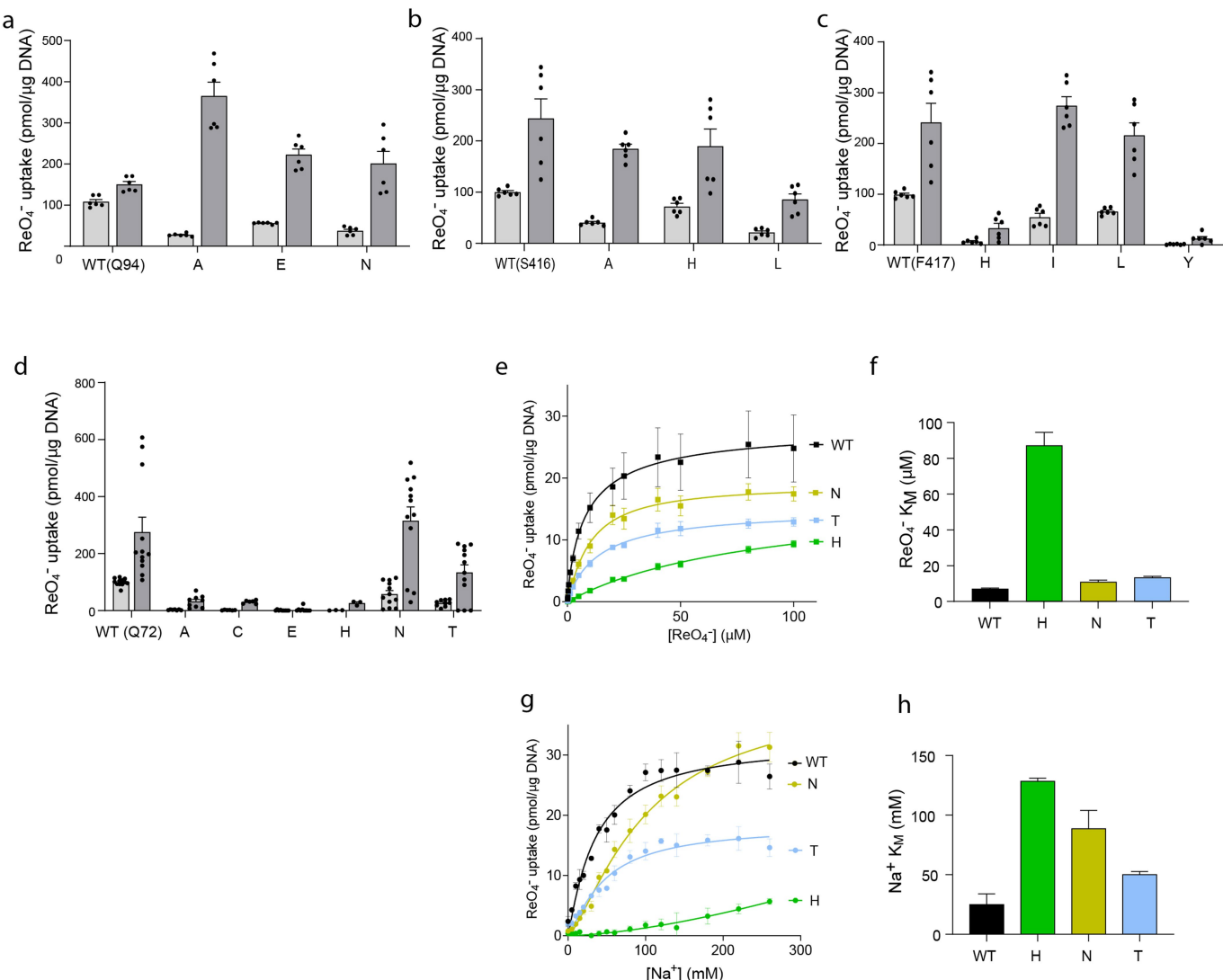
**Extended Data Fig. 5 | Effects of single amino acid substitutions at positions 69, 72, 144, 416, 417 on iodide transport.** **a–e.** NIS-mediated I<sup>-</sup> uptake at steady state. cDNA constructs coding for NIS mutants were transfected into COS7 or HEK cells. I<sup>-</sup> uptake by these NIS mutants was measured at 20 μM (light gray bars) and 200 μM (dark gray bars) I<sup>-</sup> at 140 mM Na<sup>+</sup> for 30 min with or without the NIS-specific inhibitor ClO<sub>4</sub><sup>-</sup> to determine NIS-mediated transport (values obtained in the presence of ClO<sub>4</sub><sup>-</sup>, which are <10% of the values obtained in its absence,

have already been subtracted). **f–j.** Kinetic analysis of initial rates of I<sup>-</sup> uptake (2-min time points) determined at 140 mM Na<sup>+</sup> and varying concentrations of I<sup>-</sup>. **k–o.** Kinetic analysis of initial rates of I<sup>-</sup> uptake (2-min time points) determined at varying concentrations of extracellular Na<sup>+</sup>. All results are expressed as pmol of I<sup>-</sup> accumulated/μg DNA ± s.e.m. Values represent averages of the results from two or three different experiments, each of which was carried out in triplicate ( $n \geq 6$ ).


**Extended data Fig. 6 | Identification of the ions in the NIS- $\text{ReO}_4^-$  structure.**

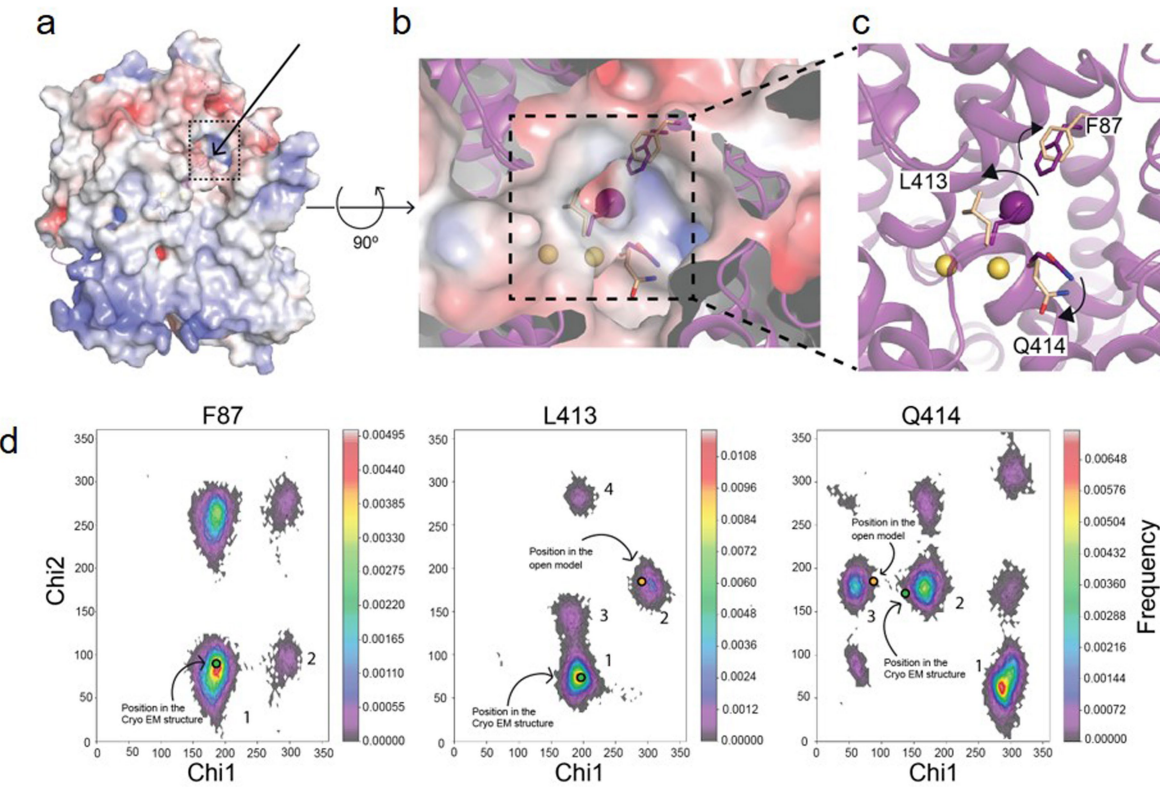
**a.** The ions transported by NIS were identified by evaluating the map density along 24 lines passing through each site (circled in yellow on images of map slices). Values are plotted for each line and the spherically-averaged mean is plotted in black (lower panels). **b.** Effects of substitutions in binding-site residues on  $\text{ReO}_4^-$  transport at steady state (measured at  $3 \mu\text{M} \text{ReO}_4^-$  and  $140 \text{ mM} \text{Na}^+$  for

30 min (values obtained in the presence of  $\text{ClO}_4^-$ , which are  $<10\%$  of the values obtained in its absence, have already been subtracted). Values are normalized to those obtained with WT NIS. Values represent averages of the results from two or three different experiments, each of which was carried out in triplicate ( $n \geq 6$ ) and reported as pmol  $\text{ReO}_4^-$  accumulated/ $\mu\text{g DNA} \pm \text{s.e.m.}$



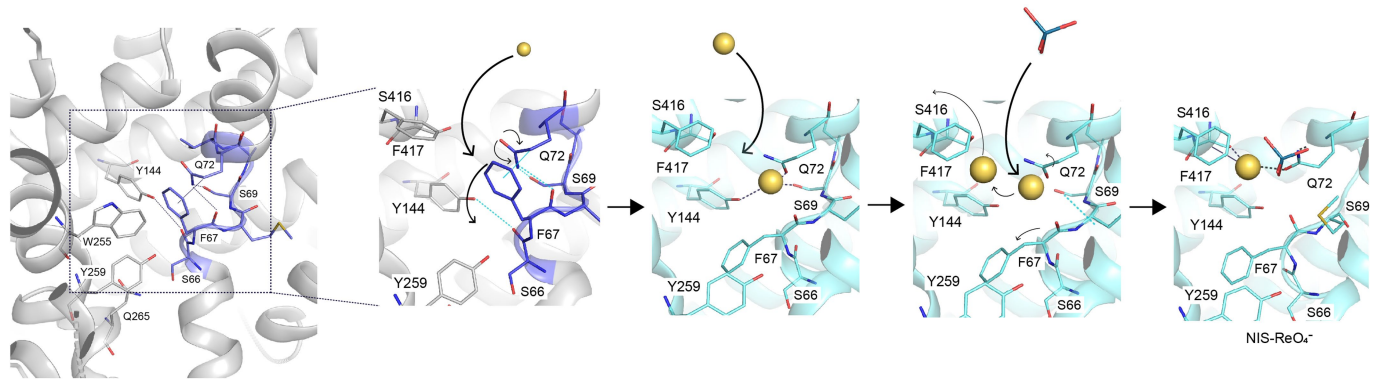
**Extended Data Fig. 7 | Effects of single amino acid substitutions at positions 72, 94, 416 and 417 on ReO<sub>4</sub><sup>-</sup> transport.** **a-d.** NIS-mediated ReO<sub>4</sub><sup>-</sup> uptake at steady state. cDNA constructs coding for NIS mutants in which Q72 is replaced with the residues indicated were transfected into COS7 or HEK cells. ReO<sub>4</sub><sup>-</sup> uptake by these NIS mutants was measured at 3 μM (light gray bars) and 30 μM (dark gray bars) ReO<sub>4</sub><sup>-</sup> at 140 mM Na<sup>+</sup> for 30 min with or without the NIS-specific inhibitor ClO<sub>4</sub><sup>-</sup> (values obtained in the presence of ClO<sub>4</sub><sup>-</sup> already subtracted). Results are given as pmols of ReO<sub>4</sub><sup>-</sup> accumulated/μg DNA ± s.e.m. Values represent averages of the results from two or three different experiments, each of which was carried out in triplicate ( $n \geq 6$ ). **e.** Kinetic analysis of initial rates of ReO<sub>4</sub><sup>-</sup> uptake (2-min time points) for Q72 NIS mutants determined at 100 μM ReO<sub>4</sub><sup>-</sup> and varying concentrations of extracellular Na<sup>+</sup>. Results are given as pmols of ReO<sub>4</sub><sup>-</sup> accumulated/μg DNA ± s.e.m. Values represent averages of the results from two or three different experiments, each of which was carried out in triplicate ( $n \geq 6$ ). **g.** Kinetic analysis of initial rates of ReO<sub>4</sub><sup>-</sup> uptake (2-min time points) for Q72 NIS mutants determined at 100 μM ReO<sub>4</sub><sup>-</sup> and varying concentrations of extracellular Na<sup>+</sup>. Results are given as pmols of ReO<sub>4</sub><sup>-</sup> accumulated/μg DNA ± s.e.m. Values represent averages of the results from two or three different experiments, each of which was carried out in triplicate ( $n \geq 6$ ). **h.** Na<sup>+</sup> K<sub>M</sub> values determined from (g); error bars represent the standard deviation of the Hill equation analysis.

extracellular Na<sup>+</sup>. Results are given as pmols of ReO<sub>4</sub><sup>-</sup> accumulated/μg DNA ± s.e.m. Values represent averages of the results from two or three different experiments, each of which was carried out in triplicate ( $n \geq 6$ ). **f.** ReO<sub>4</sub><sup>-</sup> K<sub>M</sub> values determined from (e); error bars represent the standard deviation of the Michaelis-Menten analysis. **g.** Kinetic analysis of initial rates of ReO<sub>4</sub><sup>-</sup> uptake (2-min time points) for Q72 NIS mutants determined at 100 μM ReO<sub>4</sub><sup>-</sup> and varying concentrations of extracellular Na<sup>+</sup>. Results are given as pmols of ReO<sub>4</sub><sup>-</sup> accumulated/μg DNA ± s.e.m. Values represent averages of the results from two or three different experiments, each of which was carried out in triplicate ( $n \geq 6$ ). **h.** Na<sup>+</sup> K<sub>M</sub> values determined from (g); error bars represent the standard deviation of the Hill equation analysis.



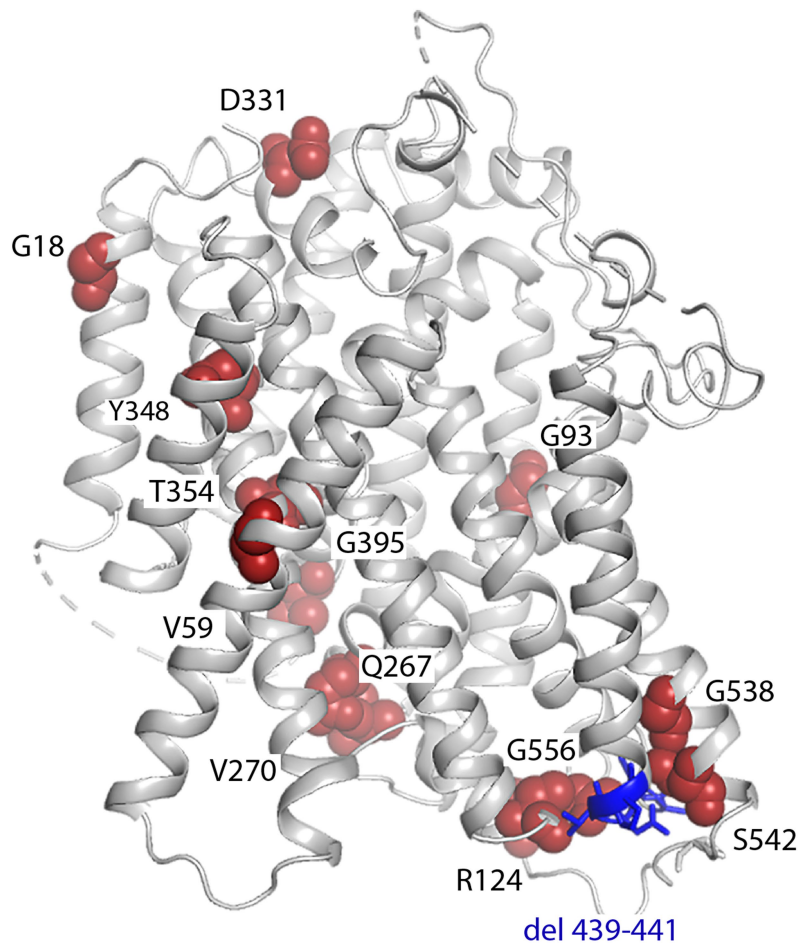
**Extended Data Fig. 8 | Entry pathway for the NIS substrates.** **a.** Surface representation of a side view of the NIS- $\text{I}^-$  structure: the arrow and the dotted square indicate the position of the proposed entry pathway. **b.** Close-up of the top view of the surface showing the substrates ( $\text{Na}^+$  ions represented by yellow spheres,  $\text{I}^-$  by a magenta sphere), and the positions of F87, L413, and Q414 in the NIS- $\text{I}^-$  structure (magenta) and the models generated from MD simulations corresponding to the opening (wheat) of the substrate-binding cavity to the extracellular milieu. **c.** Magnification of the top of the substrate-binding cavity. The arrows indicate how the amino acids move away from their original positions as the cavity transitions from closed to open. **d.** Ramachandran plots of the chi-1 and chi-2 side chain dihedral angles of F87, L413, and Q414 visited during the

MD simulations with NIS- $\text{I}^-$ . The dihedral angles selected are the principal determinants of the position of the side chain. The excursions of these dihedral angles (during the MD simulations) away from the conformational basins corresponding to the cryoEM structure (green dots in basins 1, 1, and 2, in F87, L413, and Q414, respectively) and toward conformational basins (blue dots in basins 1, 2, and 3, in F87, L413, and Q414, respectively) open up the entry path (b). In these histograms, the frequency of a given conformational state is indicated by a rainbow gradient from deep purple (0 frequency) to red (highest frequency); the most highly populated conformational basins are numbered in descending order of population.



**Extended Data Fig. 9 | Perrhenate binding mechanism starting from the apo-NIS structure.** A hydrogen-bond network between F67, S69, Q72, and Y144 and a hydrophobic stacking interaction between F67 and Q72 are disrupted by

the binding of the first  $\text{Na}^+$ . This facilitates the binding of a second  $\text{Na}^+$  and  $\text{ReO}_4^-$ , which causes the release of one  $\text{Na}^+$ .



**Extended Data Fig. 10 | Apo-NIS structure with amino acids mutated in patients with iodide transport defects shown as spheres.** Single amino acid substitutions are indicated by red spheres; deleted residues are in blue.

The substitutions found in patients are: G18R, V59E, G93R, R124H, Q267E, V270E, D331N, Y348D, T354P, G395R, G543E, S547R, G561E and the deletion of 439-443 (ACNTP).

**Extended Data Table 1 | Cryo-EM data collection, refinement and validation statistics**

	Apo-NIS (EMDB-26806) (PDB 7UY)	NIS-I <sup>-</sup> (EMDB-26808) (PDB 7UV0)	NIS- ReO <sub>4</sub> <sup>-</sup> (EMDB-26807) (PDB 7UUZ)
<b>Data collection and processing</b>			
Magnification	81,000 x	81,000 x	81,000 x
Voltage (kV)	300	300	300
Electron exposure (e-/Å <sup>2</sup> )	45	45	45
Defocus range (μm)	-1.5 / -2.4	-1.5 / -2.4	-1.5 / -2.4
Pixel size (Å)	1.068	1.068	1.068
Symmetry imposed	C2	C2	C2
Initial particle images (no.)	1.5·10 <sup>6</sup>	3.1·10 <sup>6</sup>	4.5·10 <sup>6</sup>
Final particle images (no.)	210636	384418	346284
Map resolution (Å)	3.29	3.12	3.15
FSC threshold	0.143	0.143	0.143
Map resolution range (Å)	2.8-4.0	2.3-4.2	2.5-3.4
<b>Refinement</b>			
Initial model used (PDB code)	-	-	-
Model resolution (Å)	3.4	3.3	3.2
FSC threshold	0.5	0.5	0.5
Model resolution range (Å)	n/a	n/a	n/a
Map sharpening B factor (Å <sup>2</sup> )	150	150	150
Model composition			
Non-hydrogen atoms	3808	3783	3785
Protein residues	503	501	501
Ligands	1	4	3
B factors (Å <sup>2</sup> )			
Protein	48.68	41.58	24.94
Ligand	45.88	40.74	25.30
R.m.s. deviations			
Bond lengths (Å)	0.003	0.004	0.003
Bond angles (°)	0.522	0.553	0.512
Validation			
MolProbity score	1.67	1.80	1.72
Clashscore	5.43	5.85	5.98
Poor rotamers (%)	0.25	0.51	0.51
Ramachandran plot			
Favored (%)	94.55	92.29	94.12
Allowed (%)	5.45	7.71	5.88
Disallowed (%)	0	0	0

Corresponding author(s): Nancy Carrasco

Last updated by author(s): September 27, 2022

## Reporting Summary

Nature Portfolio wishes to improve the reproducibility of the work that we publish. This form provides structure for consistency and transparency in reporting. For further information on Nature Portfolio policies, see our [Editorial Policies](#) and the [Editorial Policy Checklist](#).

### Statistics

For all statistical analyses, confirm that the following items are present in the figure legend, table legend, main text, or Methods section.

n/a Confirmed

- The exact sample size ( $n$ ) for each experimental group/condition, given as a discrete number and unit of measurement
- A statement on whether measurements were taken from distinct samples or whether the same sample was measured repeatedly
- The statistical test(s) used AND whether they are one- or two-sided  
*Only common tests should be described solely by name; describe more complex techniques in the Methods section.*
- A description of all covariates tested
- A description of any assumptions or corrections, such as tests of normality and adjustment for multiple comparisons
- A full description of the statistical parameters including central tendency (e.g. means) or other basic estimates (e.g. regression coefficient) AND variation (e.g. standard deviation) or associated estimates of uncertainty (e.g. confidence intervals)
- For null hypothesis testing, the test statistic (e.g.  $F$ ,  $t$ ,  $r$ ) with confidence intervals, effect sizes, degrees of freedom and  $P$  value noted  
*Give  $P$  values as exact values whenever suitable.*
- For Bayesian analysis, information on the choice of priors and Markov chain Monte Carlo settings
- For hierarchical and complex designs, identification of the appropriate level for tests and full reporting of outcomes
- Estimates of effect sizes (e.g. Cohen's  $d$ , Pearson's  $r$ ), indicating how they were calculated

*Our web collection on [statistics for biologists](#) contains articles on many of the points above.*

### Software and code

Policy information about [availability of computer code](#)

Data collection	SerialEM
Data analysis	Relion 3. 0 .8, MotionCor2 (1.3.1), CTFFind4.I, CryoSPARC v3.2. 0, Phenix (1.20-4459), Chimera (1.15), Coot ( 0 .9. 5), Pymol (v2), Gromacs 2020,Caver-Analyst,Origin 2021, Matlab 2020a, Clustal Omega, Jalview , FlowJo software

For manuscripts utilizing custom algorithms or software that are central to the research but not yet described in published literature, software must be made available to editors and reviewers. We strongly encourage code deposition in a community repository (e.g. GitHub). See the Nature Portfolio [guidelines for submitting code & software](#) for further information.

### Data

Policy information about [availability of data](#)

All manuscripts must include a [data availability statement](#). This statement should provide the following information, where applicable:

- Accession codes, unique identifiers, or web links for publicly available datasets
- A description of any restrictions on data availability
- For clinical datasets or third party data, please ensure that the statement adheres to our [policy](#)

Cryo-EM maps and atomic coordinates are deposited to the Protein Data Bank (PDB) databases and the Electron Microscopy Data Bank (EMDB), respectively. The accession codes are 7UUY and EMD-26806 for Apo-NIS, 7UV0 and EMD-26808 for NIS-I-, 7UUZ and EMD-26807 for NIS-ReO4- respectively, pending approval.

Reagents and other materials will be available upon request to N.C. with a completed materials transfer agreement.

The following previously published atomic coordinates were used:

PDB ID: 3DH4 [<http://doi.org/10.2210/pdb3DH4/pdb>], Crystal Structure of Sodium/Sugar symporter with bound galactose from *Vibrio parahaemolyticus*.

PDB ID: 7SLA [<http://doi.org/10.2210/pdb7SLA/pdb>], CryoEM structure of SGLT1 at 3.15 Angstrom resolution.

PDB ID: 7VSI [<http://doi.org/10.2210/pdb7VSI/pdb>], Structure of human SGLT2-MAP17 complex bound with empagliflozin.

## Human research participants

Policy information about [studies involving human research participants](#) and [Sex and Gender in Research](#).

Reporting on sex and gender

N/A

Population characteristics

N/A

Recruitment

N/A

Ethics oversight

N/A

Note that full information on the approval of the study protocol must also be provided in the manuscript.

## Field-specific reporting

Please select the one below that is the best fit for your research. If you are not sure, read the appropriate sections before making your selection.

Life sciences

Behavioural & social sciences

Ecological, evolutionary & environmental sciences

For a reference copy of the document with all sections, see [nature.com/documents/nr-reporting-summary-flat.pdf](https://nature.com/documents/nr-reporting-summary-flat.pdf)

## Life sciences study design

All studies must disclose on these points even when the disclosure is negative.

Sample size

No statistical methods were used to pre determine sample size. 108k single particle images from 8025 micrographs were used for 3D images from 3867 micrographs were used for 3D reconstructions of NIS-ReO4-. No statistical methods were used to determine sample size reconstructions of Apo-NIS. 192k single particle images from 8025 micrographs were used for 3D reconstructions of Apo-NIS. 173k single particle for EM data. These are standard sample sizes for membrane proteins of this type. Biochemical experiments were carried out in at least n=2 independent experiments with each measurement determined in triplicate, comparable to other published studies.

Data exclusions

There were no pre-established criteria for exclusion of any data. However, in the analysis of the cryo-EM data, micrographs or particles were excluded if they did not improve the map quality due to astigmatism, drift, and/or ice contamination. This is standard practice for cryo-EM structure determination.

Replication

Datasets collected on 4 different grids prepared from the same purification prep were highly similar and were combined for the final analysis. Structure determination was done once, as is standard. The numbers of independent experiments and replicates are indicated in the legends to the figures.

Randomization

The datasets were randomly split into two halves which were refined independently, is a standard step in analyzing cryo-EM data. Resolution was assessed based on the Fourier shell correlation between the half maps at the 0.143 threshold. No other randomization was attempted or needed. Randomization is not relevant for stucture determination or functional assays, because the results are not subjective.

Blinding

Blinding is not applicable to this study since the samples investigated are required to be known.

## Reporting for specific materials, systems and methods

We require information from authors about some types of materials, experimental systems and methods used in many studies. Here, indicate whether each material, system or method listed is relevant to your study. If you are not sure if a list item applies to your research, read the appropriate section before selecting a response.

## Materials & experimental systems

n/a	Involved in the study
<input type="checkbox"/>	<input checked="" type="checkbox"/> Antibodies
<input type="checkbox"/>	<input checked="" type="checkbox"/> Eukaryotic cell lines
<input checked="" type="checkbox"/>	<input type="checkbox"/> Palaeontology and archaeology
<input checked="" type="checkbox"/>	<input type="checkbox"/> Animals and other organisms
<input checked="" type="checkbox"/>	<input type="checkbox"/> Clinical data
<input checked="" type="checkbox"/>	<input type="checkbox"/> Dual use research of concern

## Methods

n/a	Involved in the study
<input checked="" type="checkbox"/>	<input type="checkbox"/> ChIP-seq
<input type="checkbox"/>	<input checked="" type="checkbox"/> Flow cytometry
<input checked="" type="checkbox"/>	<input type="checkbox"/> MRI-based neuroimaging

## Antibodies

### Antibodies used

anti-HA (YPYDVPDYA) antibody (Roche Applied Science) cat# 11867423001

### Validation

<https://www.sigmaaldrich.com/US/en/product/roche/roa-ha-ha>

## Eukaryotic cell lines

### Policy information about [cell lines and Sex and Gender in Research](#)

#### Cell line source(s)

COS-7 (ATCC), 293F (GIBCO).

#### Authentication

Cell lines were not authenticated

#### Mycoplasma contamination

Cells were not tested for mycoplasma contamination

#### Commonly misidentified lines (See [ICLAC](#) register)

No commonly misidentified cell lines were used in the study

## Flow Cytometry

### Plots

#### Confirm that:

- The axis labels state the marker and fluorochrome used (e.g. CD4-FITC).
- The axis scales are clearly visible. Include numbers along axes only for bottom left plot of group (a 'group' is an analysis of identical markers).
- All plots are contour plots with outliers or pseudocolor plots.
- A numerical value for number of cells or percentage (with statistics) is provided.

## Methodology

### Sample preparation

Paraformaldehyde-fixed cells were incubated with 0.1 µg/ml anti-HA (YPYDVPDYA) antibody (Roche Applied Science) in PBS/BSA (0.2%) followed by 50 nM of PE-conjugated goat anti-rat antibody (Life Technologies). The fluorescence of 50,000 cells per sample was assayed with a FACSCalibur flow cytometer (BD Bio-sciences). Data were analyzed using FlowJo software (Tree Star).

### Instrument

FACSCalibur flow cytometer (BD Bio-sciences)

### Software

FlowJo software (Tree Star).

### Cell population abundance

N/A

### Gating strategy

There is no gating strategy. Cells transfected with empty plasmid (i.e., not containing the cDNA of interest) were used as negative controls.

Tick this box to confirm that a figure exemplifying the gating strategy is provided in the Supplementary Information.